THE BRAIDED JETS IN THE SPIRAL GALAXY NGC 4258

GERALD CECIL
Department of Physics and Astronomy, University of North Carolina, Chapel Hill, NC 27599–3255

ANDREW S. WILSON[1]
Astronomy Department, University of Maryland, College Park, MD 20742

AND

R. BRENT TULLY
Institute for Astronomy, University of Hawaii, Honolulu, HI 96822
Received 1991 May 8; accepted 1991 October 15

ABSTRACT

We have used the Hawaii Imaging Fabry-Perot Interferometer to synthesize 44,000 Hα and [N II] emission-line profiles at velocity resolution 68 km s^{-1} FWHM across the disk of the nearby Seyfert/LINER galaxy NGC 4258, including the prominent "four-branched jet" that extends to 10 and 5 kpc radii in the radio continuum and optical emission lines, respectively. A long-slit spectrum, which includes the emission lines Hα, [N II] $\lambda\lambda$6548, 6583 and [S II] $\lambda\lambda$6717, 6731, has also been obtained along the jets. These data are used for a comprehensive kinematic study of the galaxy.

The disk velocity field is best fitted with a model that incorporates elliptical, bar-forced streaming motions, as suggested by the H I and CO kinematics. Velocity dispersions along the SE jet average 80 km s^{-1}, compared to 40 km s^{-1} in the H II regions. This broadening arises from a helical, braided structure of three intertwined plasma streams, as inferred from both the spatial and kinematic structure of the jet. The emission-line profiles split into two distinct velocity systems with separations 300 ± 30 km s^{-1} within 1.7 kpc of the nucleus along the midaxis of the braid pattern. Gaussian decomposition of the line profiles show that the internal velocity dispersion of each helical strand is $\approx$100 km s^{-1}. We observe two cycles of the triple-braid pattern, with wavelength $\approx$1.4 kpc and side-to-side amplitude $\approx$400 pc. If the braided streams represent ballistic motion of gas ejected from orbiting objects, the outflow velocity is $\approx$2000 km s^{-1}. The masses and separations of the compact objects would be $\approx$3 × 10^6 $M_\odot$ and $\approx$6 pc (0″.2), respectively. However, the emission-line velocity field of the SE jet suggests that the gas moves *along* the helices, perhaps as a result of fluid instabilities at the interface between the jet and the interstellar medium or of motion along magnetic flux tubes. We show that the NNW jet follows a clear channel between molecular cloud complexes, and exhibits several emission-line "hot spots" and bends where it interacts with the surrounding molecular gas. High-velocity gas in the SE and NW radio "plateaus" probably results from earlier ejections of gas from the nucleus in these directions, with the jet nozzle having precessed to its present orientation. We find that the jets have total ionized mass 1.5 × 10^6 $M_\odot$ (1 cm^{-3}/n_e) and [N II] λ6583/Hα ratios consistent with shock excitation. An *Einstein* HRI image reveals X-ray emission from the nucleus and SE jet. We show that the jet's X-ray emission may be interpreted as thermal bremsstrahlung from hot, shocked jet gas.

Subject headings: galaxies: individual (NGC 4258) — galaxies: ISM — galaxies: jets — galaxies: kinematics and dynamics — magnetic fields — X-rays: galaxies

1. INTRODUCTION

The nearby SABbc galaxy NGC 4258 (7 Mpc distance, hence 1″ = 35 pc; Tully 1988) exhibits a well-known (e.g., Martin et al. 1989, hereafter MRNL, and references therein) pair of "anomalous arms," visible in Hα and radio continuum, that are quite distinct in morphology and gaseous excitation from the normal spiral arms delineated by H II regions. These anomalous arms, which are usually interpreted in terms of collimated nuclear outflows or "jets," emerge from the nuclear region as linear features, then bend at 2–5 kpc radius in a trailing sense with respect to galactic rotation. The absence of blue continuum emission cospatial with the jets shows that OB stars are not responsible for the gaseous excitation.

Van der Kruit (1974) inferred complex velocity patterns and anomalous gaseous excitation from many optical long-slit spectra obtained across the inner disk and jets. However, van

Albada (1980, hereafter VA) used λ21 cm H I observations of comparatively low spatial resolution (21″ FWHM) to show that the disk exhibits noncircular motions that are consistent with those expected from the dynamical effects of a stellar bar, with no evidence for strong kinematic deviations near the jets. The *Einstein* HRI image of this galaxy has recently been published without comment by Fabbiano, Kim, & Trinchieri (1991). We show that much of the X-ray flux is associated with the SE jet. Ford et al. (1986) have remarked on the "braided" appearance of the jets in their Hα + [N II] $\lambda\lambda$6548, 6583 images, suggesting that the plasma streams twist around one another. With the exception of luminous water masers (Claussen, Heiligman, & Lo 1984) and a weak broad-line component in the Hα line profile (Stauffer 1982; Filippenko & Sargent 1985), the nucleus appears relatively quiet at present.

Recently, MRNL have found that the innermost Hα and CO flux distributions are spatially *anti*correlated. They argued from this observation that the nuclear outflow is still active

---

[1] Also Space Telescope Science Institute.

and has excavated a channel in the ambient interstellar medium (ISM). From the detailed morphology of the Hα emission, MRNL identified several regions where the interaction between the outflow and the ISM appears particularly strong. Plante et al. (1991, hereafter PLRMN) find evidence in the CO velocity field for "bar-forcing" and for an interaction between the jet and the ISM NNW of the nucleus.

These processes are basic to our understanding of jets and associated ionized gas in Seyfert galaxies, radio galaxies and quasars. The proximity of NGC 4258, and consequent favorable spatial scale, makes this nuclear outflow an important laboratory for study of both jet/ISM interactions and the influence of a bar on gas flows that could fuel an active nucleus. In this paper we present imaging spectrophotometry of the [N II] λ6583 and Hα emission lines across the disk of NGC 4258. Our data isolate the jets kinematically, spatially, and by the gaseous excitation from the adjacent, rotating disk gas. We describe the acquisition and reduction of Fabry-Perot data and a complementary long-slit spectrum in § 2. Our results are presented and interpreted in terms of various kinematic models in § 3. Based on more extensive kinematic modeling, our intrepretation supersedes the preliminary report of Cecil (1991). In § 4 we discuss the dynamical implications and interpret the published *Einstein* HRI image in terms of thermal bremsstrahlung from the jets. We summarize in § 5.

2. OBSERVATIONS AND REDUCTIONS

2.1. *Imaging Fabry-Perot Spectrophotometry*

We used the Hawaii Imaging Fabry-Perot Interferometer (HIFI: Bland & Tully 1989) and a low-noise ($5e^-$ rms readout), thick epitaxial GEC CCD to obtain a total of 59 nine minute exposures in photometric conditions over several hours on each of 1988 May 14 and 15. The CCD/HIFI combination was attached at the Cassegrain focus of the University of Hawaii (UH) 2.2 m telescope at the Mauna Kea Observatory. The pixel scale was 0″.85 with the f/2.4 beam. Additional exposures were made of photometric standard stars to provide an absolute flux calibration. A finesse 60 etalon with free spectral range 87 Å at Hα was used in its 75th order to yield a velocity resolution of 68 km s^{-1} (FWHM). An order separating filter with a flat-topped transmission profile and 50 Å FWHM bandpass passed only one etalon order, so true emission-line profiles could be synthesized. Wavelength coverage was such that predominantly Hα emission was recorded on the first night and [N II] λ6583 on the second, at 36 km s^{-1} velocity increments.

The extreme blueward wavelengths of our spectra were attenuated by the filter transmission profile. normally, the dome flat fields permit correction for this effect, but illumination differences led to an overcorrection in the N part of our data cube. Fortuitously, gas motions in the galaxy redshift the kinematic structure away from this part of the spectrum, and we were able to obtain good fits to Hα profiles across the entire field. However, because of the limited range of wavelengths observed, we did not reach the continuum at all locations, incompletely sampling the red wing of the [N II] λ6583 profile NW of the nucleus and the blue wing of Hα in regions of high-velocity gas to the SE.

The neon line at 6598.95 Å was observed from a calibration lamp to monitor wavelength drifts during the early part of each night. Drifts occurred because of a mismatch in thermal time constants between the glass etalon and the embedded air gap.

HIFI was not thermally regulated at the time of these observations, although the gap was flushed with dry nitrogen gas to minimize changes in refractive index. The wavelength drift leads to changes in the radii of rings of night sky line emission, and is noticeable between the two nights because we began observations at different times in the diurnal temperature cycle.

To minimize other time-dependent systematics, the central wavelengths of the individual images were ordered so as to scan each emission line in a random sequence. The only noticeable instrumental effect was an EW oscillation of amplitude 1″.8 in the telescope tracking during part of the second night. Six of the frames taken then were visibly trailed, but the effect on the whole line profile is minor.

After subtraction of the electrical bias offset and interpolation over a few columns with poor charge transfer, the individual images were stacked into a data cube that samples the [N II] λ6583 and Hα lines. The data cube was calibrated and analyzed on Sun 4 workstations using locally developed software. Calibration of this cube was similar to the one obtained on NGC 1068 (see Cecil, Bland, & Tully 1990); here we outline only the special processing required for the present data.

We first fitted and removed rings due to sky line emission in each image. Although residual sky lines limit our dynamic range, the reality of faint kinematic substructure can be established by verifying that it appears in both the Hα and [N II] λ6583 profiles. The continuum sky level of each frame was then determined from the median of several areas relatively free of galaxy light and subtracted from the image. All images were then aligned using field stars (drifts were a few pixels at most), and subsequent automated processing treated each spectrum separately in the resulting two-dimensional spatial grid.

To correct for the temperature-induced velocity drifts established from the sky lines, the spectra were first interpolated to uniform wavelength sampling by means of a sinc-function. Next, the data were interpolated again to correct for the curvature of the isovelocity surfaces ("nested paraboloids"), so that spectral profiles at different points in the cube could be easily intercompared without reference to this "phase surface" (Bland & Tully 1989). The heliocentric velocities of residual night-sky emission lines, as given by Rubin & Graham (1990), confirmed the velocity calibration. We removed cosmic-ray tracks by median filtering each spectrum above an empirical threshold.

We parameterized the spectrophotometric content of our cube by fitting Gaussians to the spectral lines, assuming a flat continuum at each location. The continuum near the nucleus was set at the lowest point in the observed spectrum, because the emission-lines here are broader than our velocity coverage. Thus, line fluxes are slightly underestimated in these regions. The use of different weighting schemes led to no significant differences in the fits. Gaussian functions are inappropriate descriptors of the line profiles along the jets near the nucleus, because both the [N II] λ6583 and Hα profiles are double-peaked on both sides of the nucleus (e.g. Rubin & Graham 1990). Although the velocity centroid adequately summarizes the gross kinematics of this gas, the complex flow field is most effectively established from more detailed analysis of our line profiles (see § 3.2).

Poor Gaussian fits to the line profiles were identified through their abnormal velocity centroids, widths, and continuum levels, and then deleted. The map of the flux ratio [N II] λ6583/Hα also allowed identification of bad fits, because this

ratio is always <0.5 in H II regions. The luminous H II complex at the southern extremity of the field was reflected across the etalon optical axis in frames where it is bright. This spurious ghost image is sufficiently strong to dominate the emission-line profiles, so we did not attempt fits in this region (denoted "G" in Fig. 2c). We have, however, corrected the flux map for this feature.

In all, reliable Gaussian fits were made to nearly 16,000 Hα and 7400 [N II] $\lambda6583$ profiles. Regions with good fits were then masked and the remainder of the cube was spectrally smoothed with an eight element, fourth-order Savitzky-Golay filter (e.g. Press & Teukolsky 1990), to improve the sensitivity to fainter features. This allowed us to establish the kinematics of about 21,000 more profiles, by measuring their intensity-weighted spectral moments over the velocity range defined by the successful Gaussian fits in adjacent pixels. The aim of this extrapolation was to establish the gross structure of the large-scale gas disk, so that its kinematics and flux distribution could be more reliably constrained (see § 3.1). Our 5' field and the distribution of ionized gas within this galaxy permits measurement of the gaseous kinematics to a maximum radius in the disk of 9.5 and 5 kpc along the minor and major axes, respectively.

Figure 1 compares the velocity centroids derived from the two emission lines; the insert shows that the FWHM of the histogram of velocity differences is 36 km s^{-1}. This value is larger than expected, indicating a true difference in the [N II] $\lambda6583$ and Hα velocity fields. The centroid of the histogram is at -10 km s^{-1}, which may reflect residual errors due to temperature drift. Examination of Figure 1 suggests that much of the velocity difference between the two lines arises from a systematic deviation of $V(H\alpha) - V([N\ II]\ \lambda6583) \approx -25$ km s^{-1} at velocities between 250 and 350 km s^{-1}, which correspond to the SE jet. Ignoring this region, Figure 1 indicates a velocity accuracy of 20 km s^{-1} rms. Van der Kruit (1974) found no discernible difference in the two velocity fields at similar velocity resolution, but he did not explicitly discuss differences across the SE jet.

The instrumental spectral throughput was established from fluxed observations of NGC 6240 (Bland-Hawthorn, Wilson, & Tully 1991) that were made later in the night. Observed fluxes have not been corrected for Galactic reddening (reported to be negligible) or internal reddening, despite evidence for widespread dust in NGC 4258 (§ 2.3). Hα luminosities were established assuming a distance of 7 Mpc, and converted to
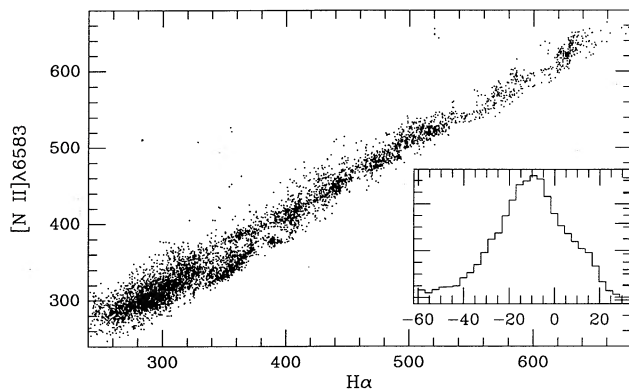

FIG. 3.—Hα luminosity of the gas disk within each 10 km s^{-1} wide velocity bin [in units of $10^5\ M_\odot\ (1\ cm^{-3}/n_e)$], with $V_{helio} = 464$ km s^{-1} as the origin of the velocity scale.

units of $M_\odot\ (1\ cm^{-3}/n_e)$, with n_e the electron density, by assuming case B recombination conditions at 10^4 K (e.g., Osterbrock 1989). This assumption may be incorrect for the jet if the gas is ionized by shock waves. The total Hα luminosity from regions with measurable flux is 7.6×10^{39} ergs s^{-1}, corresponding to $1.7 \times 10^7\ M_\odot\ (1\ cm^{-3}/n_e)$ (<1% of the total H I mass; VA). We find that the ionized mass of the active jets is $2.4 \times 10^6\ M_\odot\ (1\ cm^{-3}/n_e)$, which is only 6% of that estimated by MRNL (who did not have absolute fluxes and who used too large a jet width). Filippenko & Sargent (1985) show the nuclear spectrum but do not report absolute fluxes. Figure 2 (Plate 1) shows maps of selected parameters.

Figures 3–5 summarize some aspects of our data cube. Figure 6 plots velocities measured by simulated long-slit spectra in the position angles obtained by Rubin & Graham (1990), and shows good agreement with their Figure 2. A simulated long-slit spectrum along P.A. 145° agrees with that of Dettmar & Koribalski (1990), and our [N II] $\lambda6583$/Hα ratios also agree with their values SE of the nucleus, where we have complete nitrogen profiles.

2.2. Long-Slit Spectrum

To further constrain the properties of the extranuclear gas, a 1 hr exposure long-slit spectrum was taken on 1985 February

FIG. 1.—Comparison of the Hα and [N II] $\lambda6583$ heliocentric velocities (in km s^{-1}) south of the nucleus where we scanned the nitrogen line. The insert shows a histogram of $V(H\alpha) - V([N\ II]\ \lambda6583)$ (in km s^{-1}).
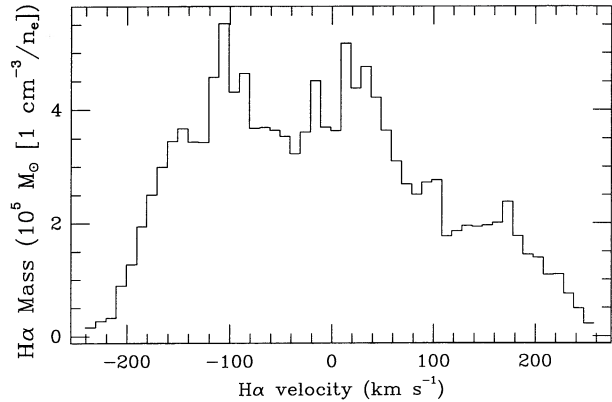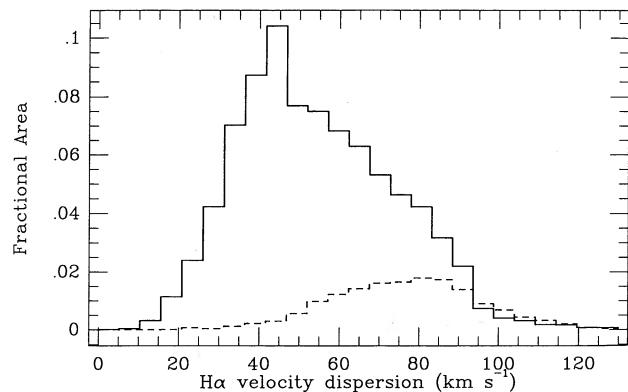

FIG. 4.—Histograms of the Hα velocity dispersion in 5 km s^{-1} wide bins, corrected in quadrature for an instrumental resolution of 68 km s^{-1} (FWHM), and normalized by fractional area over the galaxy. The peak at 41 km s^{-1} corresponds to H II regions in the normal spiral arms. The dashed curve shows the histogram for the jets; the solid histogram, for the rest of the disk.

PLATE 1

2.0
0.5
0.2

jets

0.8
0.5
0.2

2 kpc

(a) H⁺ Mass

(b) [N II]/Hα

700
600
500 km/s
400
300

jet

G

90
50 km/s
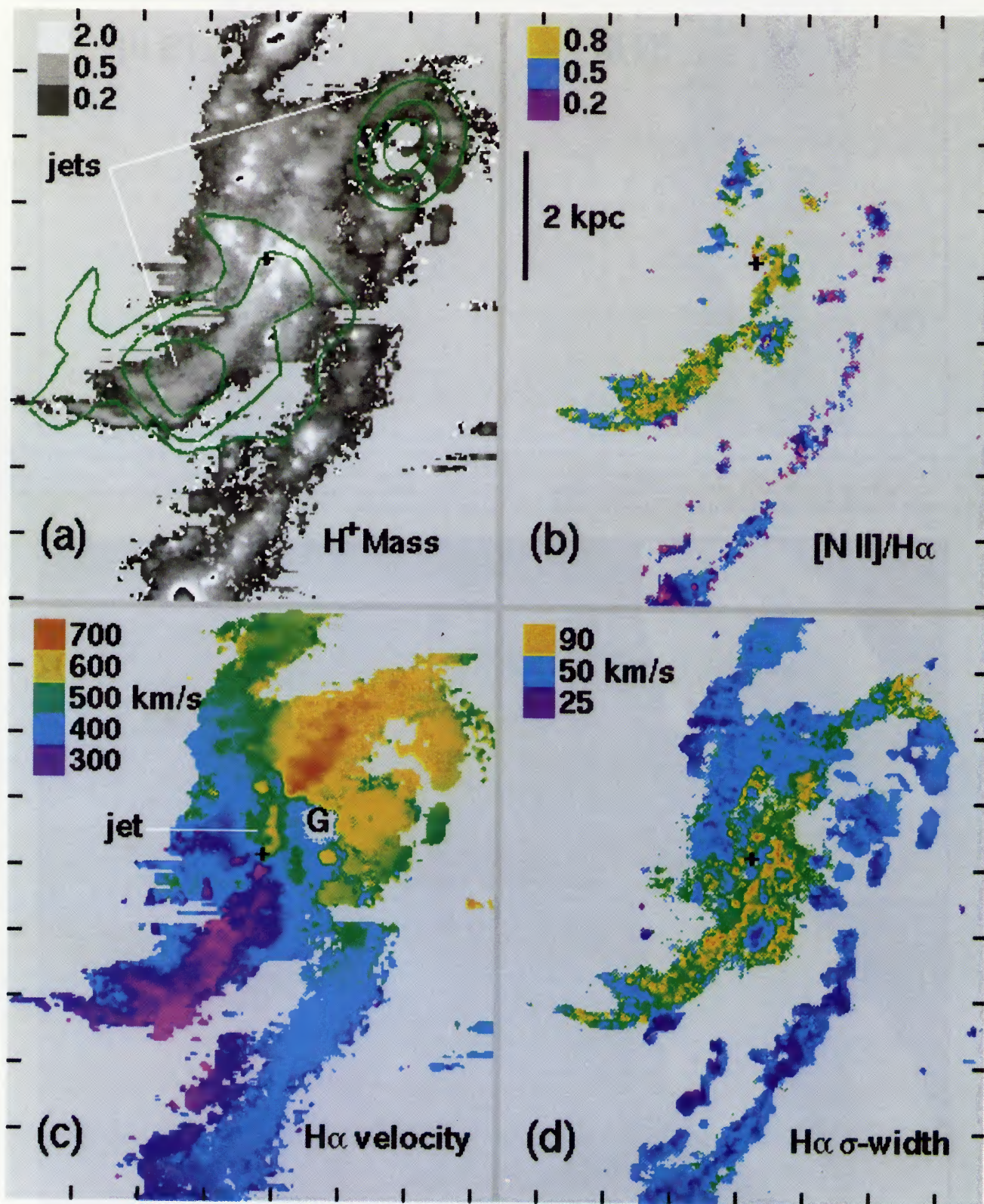**25**

(c) Hα velocity

(d) Hα σ-width

FIG. 2.—Maps derived from nearly 45,000 Gaussian fits or spectral moments. The points plotted in (d) were derived from Gaussian fits. The additional points plotted in (a) and (c) were derived from spectral moments after smoothing (see text). N is up and E is at left; ticks at 1.2 kpc (36″) increments; plus sign at the nucleus. The gray scale wraps through white in the brightest regions. A reflective ghost was subtracted at "G". (a) Hα luminosity distribution (log scaled) in units $M_\odot \; \mathrm{pc}^{-2}$ $(1 \; \mathrm{cm}^{-3} \; n_e^{-1})$. The green contours show the distribution of soft X-ray emission from the *Einstein Observatory* HRI (data from Fabbiano et al. 1992, smoothed to $\sigma = 16''$); note the coincidence with the SE jet. (b) [N II] $\lambda 6583$/Hα flux ratio. Note the abnormally high values associated with the SE jet. (c) Hα velocity field, with 36 km s⁻¹ sampling and 68 km s⁻¹ FWHM (heliocentric systemic velocity = 464 km s⁻¹), and spatially smoothed to 1″.7 FWHM. (d) Hα velocity dispersion, corrected in quadrature for instrumental resolution. The large widths along the SE jets arise from the putative helical gas motions.
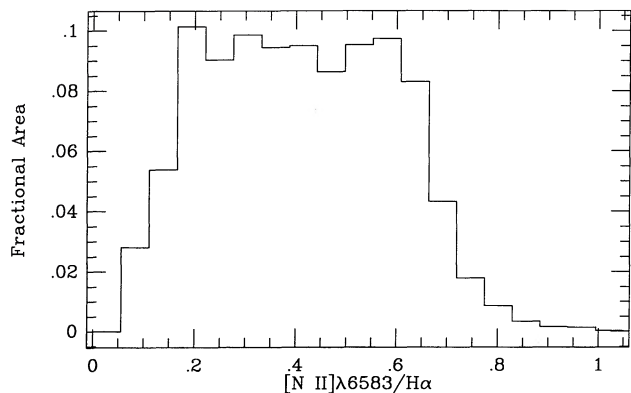
Cecil, Wilson, & Tully (see 390, 367)

FIG. 5.—Histogram of [N II] $\lambda 6583$/Hα values south of the nucleus (where the nitrogen line was parameterized; see Fig. 2b), normalized by the fractional area over the galaxy. Values >0.5 (in the extended tail of the distribution) are associated with the jets.

13 with the UH 2.2 m telescope and the Institute for Astronomy (IfA) Faint Object Spectrograph (FOS). The conditions were not photometric (broken cirrus clouds) and the seeing was 1″8 FWHM. The 1″5 wide × 87″ long slit was placed close to the nucleus along the SE jet (and kinematic major axis) at P.A. 150°. The IfA/Galileo CCD system was used with a UV-flooded, three-phase, backside-illuminated, thin 500 × 500 Texas Instruments CCD ($22e^-$ rms readout noise). A 1200 grooves mm^{-1} grating, blazed at Hα, was used in first order to cover the wavelength range $\lambda\lambda 6400$–6900 with resolution of 2.5 Å FWHM and spatial sampling 0″76 pixel^{-1}. Slit spatial registration and pixel scale were established with a broad-band image made with the FOS in its imaging mode immediately before the spectrum exposure. We estimate that the slit was centered within 1″ of the nucleus. The internal FeAr lamp was used to calibrate the wavelength scale, and night sky lines confirmed the velocity solution. A dome flat-field image immediately after the exposure allowed calibration of pixel-to-pixel variations. The stellar continuum was established at each point along the slit with a linear least-squares fit through line-free portions of the spectrum. Finally, the spectrum was smoothed with $\frac{1}{4}$–$\frac{1}{2}$–$\frac{1}{4}$ weights along the spatial dimension.

Figure 7a (Plate 2) shows the region of interest after sky and galaxy continuum subtraction. Note the regular *kinematic* braiding of the jet SE of nucleus, the "turbulent" appearance NW, and profile splitting of up to 330 km s^{-1}. The variations of the Hα and [N II] $\lambda 6583$ velocities and the [N II] $\lambda 6583$/Hα ratio along the slit all agree to within the errors with those extracted from the Fabry-Perot data cube along P.A. 150° and with the major axis spectrum of Dettmar & Koribalski (1990). The absolute velocities also agree well with those of Rubin & Graham (1990).

2.3. CCD Broad-Band Images

M. Pierce kindly provided us with B and I images of NGC 4258, made with the 0.6 m Planetary Patrol Telescope at Mauna Kea Observatory and the same CCD that we used for our long-slit spectrum. A focal reducer was used to obtain a pixel scale of 1″6 across a field 13′ square. The images were calibrated with dome flats and photometric standard stars. A telescope malfunction slightly trailed the 10 minute, unguided exposures, so we smoothed the frames with elliptical Gaussians to a circular beam of 8″ FWHM. Photometric profiles of the

galaxy will be presented elsewhere (M. Pierce, in preparation). We subtracted the logarithmically scaled images to produce a $B-I$ magnitude color map (Fig. 8 [Pl. 2]). This shows red dust bands associated with the nuclear CO complex discussed by MRNL, as well as strong blue light in the normal spiral arms. The jets are invisible in these predominantly continuum images, as others have noted.

3. KINEMATICS OF THE IONIZED GAS

We must first model the well-documented noncircular motions in the disk of NGC 4258 (e.g., VA and references therein; PLRMN) before we can isolate the kinematic effects of the jets. Plausible dynamical origins of the motions include forcing by the inner stellar oval or bar, density wave streaming associated with a nonaxisymmetric spiral arm in the southern half of the galaxy, and warpage of the large-scale H I disk. Our observations refer to much smaller radii than the H I extent, so the last effect is presumably unimportant.

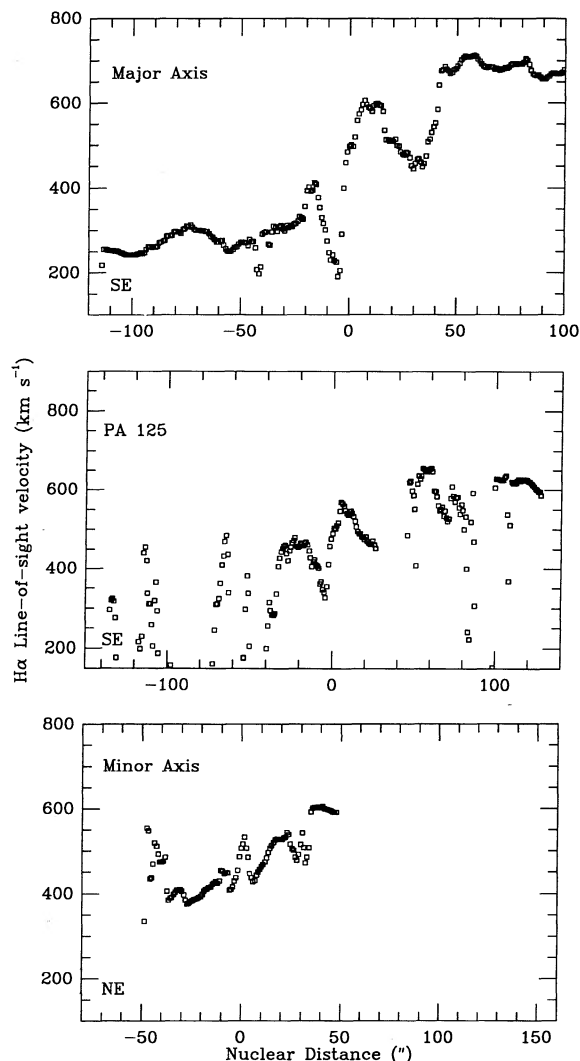FIG. 6.—Hα velocities extracted from the data cube in a 2″ wide slice through the nucleus along P.A. (*top*) $-30°$ (major axis), (*middle*) 125° (data between 30″ and 45″ are unreliable because of a reflective ghost, so are not shown), and (*bottom*) 60° (minor axis), in order to simulate conventional long-slit spectra. These plots may be directly compared with Fig. 2 of Rubin & Graham (1990).
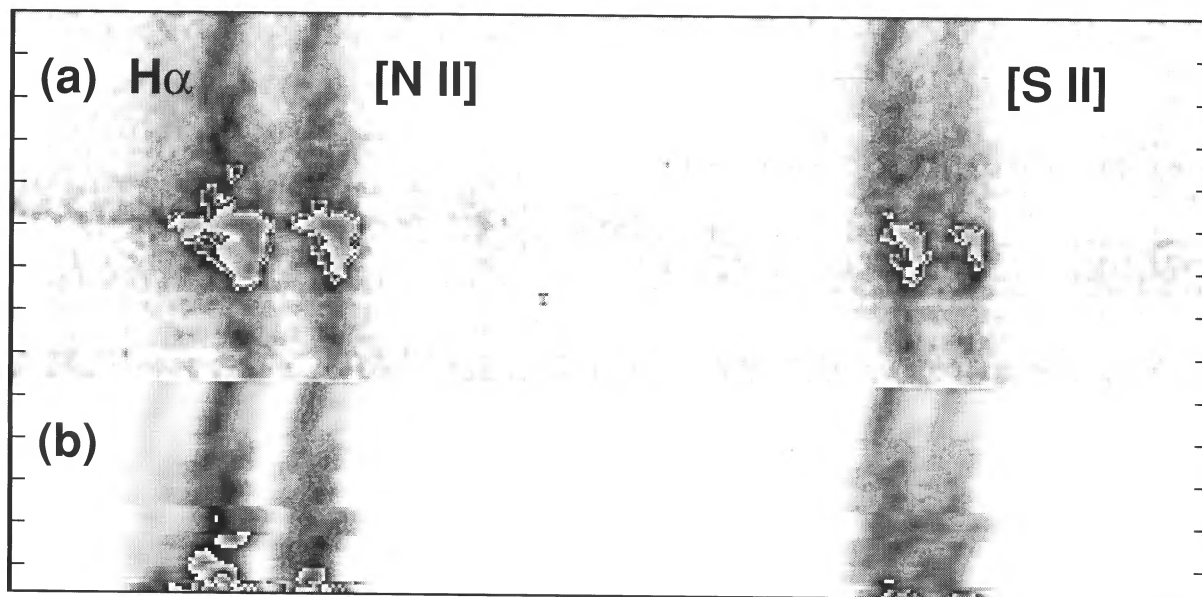
PLATE 2

FIG. 7.—(a) The long-slit spectrum, including the Hα, [N II] λλ6548, 6583 complex and [S II] λλ6717, 6731 doublet at 0″.76 increments along 150° P.A., after continuum subtraction. The broadest lines are at the nucleus. SE is at the top, NW is at the bottom, and ticks are every 375 pc (11″). Note the repetitive pattern along the slit to the SE of the nucleus. (b) Fit to all line profiles simultaneously, assuming two Gaussian subsystems in each line at each location SE of the nucleus. The repetitive pattern along the slit is well described by this parameterization. The fit parameters are plotted in Fig. 14.
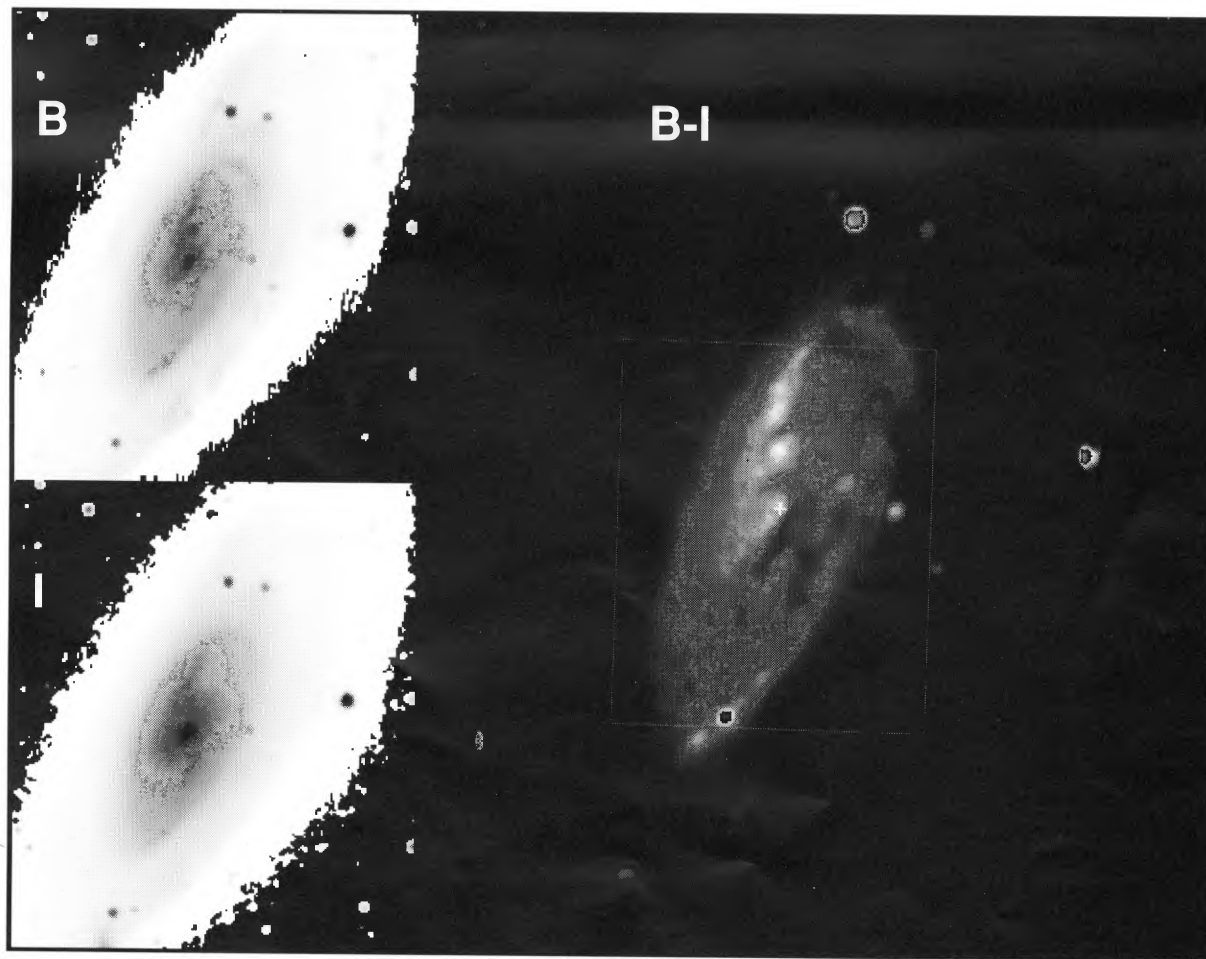

FIG. 8.—Broad-band CCD images of NGC 4258, smoothed to 8″ FWHM. The field is rotated 1°.5 counterclockwise from an orientation with north at top and east at left. The logarithmically scaled images on the left cover ≈13′ × 13′ and were subtracted to produce the linearly scaled B − I color map on the right shown at twice the scale. The gray scale of the color map shows "blue" regions as white. The box (with cardinal orientation) circumscribes the region covered by our Fabry-Perot data cube, and the plus sign marks the nucleus. Note the dark dust bands near the nucleus.

CECIL, WILSON, & TULLY (see 390, 368)

A self-consistent dynamical interpretation requires analysis of the surface photometry to constrain the mass distribution, a task beyond the scope of this paper. The jets lie close (at least in projection) to the major axis of the galaxy disk, so our modeling of the underlying rotational velocity field will require minimal corrections for spatial projections, but will be insensitive to any radial motions within the disk along the jet axis. We focus our discussion on the velocity centroids from our Gaussian fits (Fig. 2c). Our data provide constraints only to a maximum radius of 9.5 kpc and minimum of 100 pc ($\approx 3''$). The velocities at large radii result from measurements close to the minor axis because of the high inclination of NGC 4258.

3.1. The Velocity Field of the Ionized Disk

Van der Kruit (1974) and VA agree on the kinematic major axis (P.A. = $148° \pm 2°$) but not on the rotation curve. VA's H I $\lambda 21$ cm observations have complete spatial coverage but do not strongly constrain the rotation curve at radii less than 1 kpc because of their lower spatial resolution ($20''$ vs. $3''$ FWHM for van der Kruit's measurements). Van der Kruit (1974) finds strong deviations from an axisymmetric model in the emission-line gas throughout the nuclear region, but VA's H I map shows no kinematic deviations across the jets, other than effects that he attributes to forcing by the stellar bar. Rubin & Graham (1990) find significant differences between the major axis rotation curves on either side of the nucleus. In this section, we attempt to quantify the effects of the bar.

We began our analysis by generating a model velocity field using VA's axisymmetric disk parameters (including his inclination $i = 72°$), a cubic spline fit to his rotation curve number 2, and his estimated systemic velocity of 450 km s^{-1}. Figure 9a shows both this model and the result of subtracting it from our measured Hα velocity field. Overall, the model describes well the kinematics of the outer spiral arms, but there are differences of up to 150 km s^{-1} between our data and this model at smaller radii in all quadrants. The residuals are slightly reduced by altering the inclination, kinematic major axis, and systemic velocity to $i = 64°$, P.A. $= 146°$, and 467 km s^{-1} respectively (i.e., van der Kruit's 1974 parameters).

However, the underlying cause of all the residuals might plausibly be distortion of the gas orbits by bar-forced, elliptical streaming. The bar's influence is also apparent in the H I $\lambda 21$ cm velocity field (Fig. 6 of VA). As VA has noted, even weak noncircular motions associated with the bar could mimic a jet outflow near the kinematic major axis. In fact, PLRMN find nonrotational motions in their near-nuclear velocity field from CO measurements, consistent with bar-streaming together with 45 ± 15 km s^{-1} of expansion within $15''$ radius. They modeled the bar-induced elliptical orbits as having constant eccentricity and major axis P.A., a simplification justified by the limited spatial extent of the detected CO emission.

The H I flux distribution (VA) and CO kinematics near the nucleus (PLRMN) both suggest that the bar's major axis is oriented at P.A. $17° \pm 3°$ (which is $74° \pm 2°$ from the kinematic major axis in the disk plane), and that the bar has ellipticity $e = 1 - b/a = 1 - \epsilon \approx 0.35$ (i.e., axial ratio $a:b = 3:2$). The good fit of the axisymmetric model to the H I velocity field suggests that the gas orbits must be approximately circular outside 7.6 kpc radius. To isolate the kinematic effects of the jets themselves, we therefore construct more elaborate models of gas motions in the inner disk, similar to those described in Staveley-Smith et al. (1990), but differing in detail from those of PLRMN. We model the intrinsic gas orbits as nonintersecting,

inclined elliptical annuli that conserve angular momentum (so there are no hydrodynamic shocks, or gas flows associated with the unstable stellar orbits that form near the corotation radius; Teuben & Sanders 1985). Ellipticity variations with radius are conveniently parameterized as

$$\epsilon(r) = \pi^{-1}(1 - \epsilon_0) \arctan [q(r - r_b)] + (1 + \epsilon_0)/2$$

with r and r_b in kpc. With this form, the orbit ellipticities decrease smoothly from $1 - \epsilon_0$ at small radii to 0 when $r \gg r_b$. Adopting $r_b = 7.6$ kpc and fitting this model to our Hα velocity field, we estimate $\epsilon_0 = 0.6$ and $q = 8$ kpc^{-1}. Our estimate for the heliocentric systemic velocity, 464 ± 4 km s^{-1}, is essentially that of van der Kruit (1974) and Rubin & Graham (1990), but different from that of VA. Ionized gas is not distributed over the whole disk, so the amplitude of our rotation curve can be more than 15 km s^{-1} below that of VA to compensate for our larger systemic velocity. Moreover, variations in the bar eccentricity can be "played off" against the form of the rotation curve and, because we did not exhaustively search parameter space, some improvement over our fits may be possible. For example, the kinematic and photometric centers may not coincide. Without a self-consistent dynamical framework, our kinematic model only illustrates a plausible bar response consistent with the H I flux distribution and the H I and CO kinematics.

Compared to the model with purely circular motions (Fig. 9a [Pl. 3]), the velocity residuals from the model incorporating elliptical streaming (Fig. 9b [Pl. 3]) are significantly smaller W of the nucleus and somewhat smaller beyond $30''$ radius, but remain large near the nucleus (cf. Fig. 9c [in text]). These trends are stable to reasonable variations about our assumed values of the eccentricity function, rotation curve, and projection angles. Adding purely radial motions within the disk near the nucleus, and of the magnitude favored by PLRMN, fails to improve the fit because the residuals along the minor axis have the same sign on both sides of the nucleus. The residuals could be reduced with an ad hoc decrease in disk inclination near the nucleus (e.g., Fig. 1 of van der Kruit & Allen 1978), relative to the inclination of the putative, warped (VA) outer disk. Alternatively, the persistent kinematic deviation S of the nucleus to a radius of $\approx 35''$ (denoted "S" in Fig. 9b) might arise from the shocks that form along the leading edges (in the sense of galactic rotation) of a bar (Roberts,
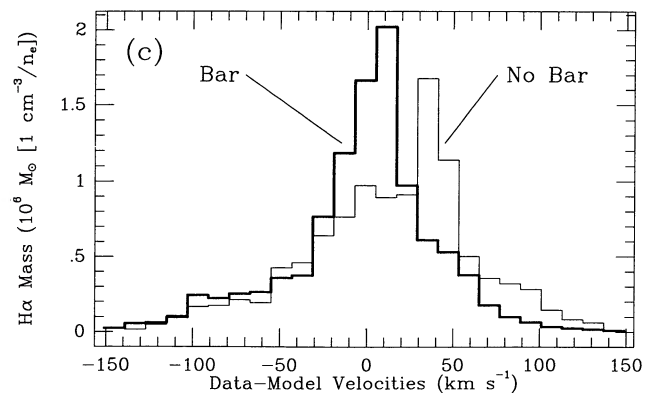

FIG. 9c.—Histogram showing Hα luminosity [in units of $10^6 M_\odot$ pc^{-2} (1 cm$^{-3}/n_e$)] as a function of residual velocities (data-model) for the models in Figs. 9a and 9b (in plate section). Note that the centroid of the profiles that are associated with the jets all deviate < 60 km s^{-1} from the ambient disk.
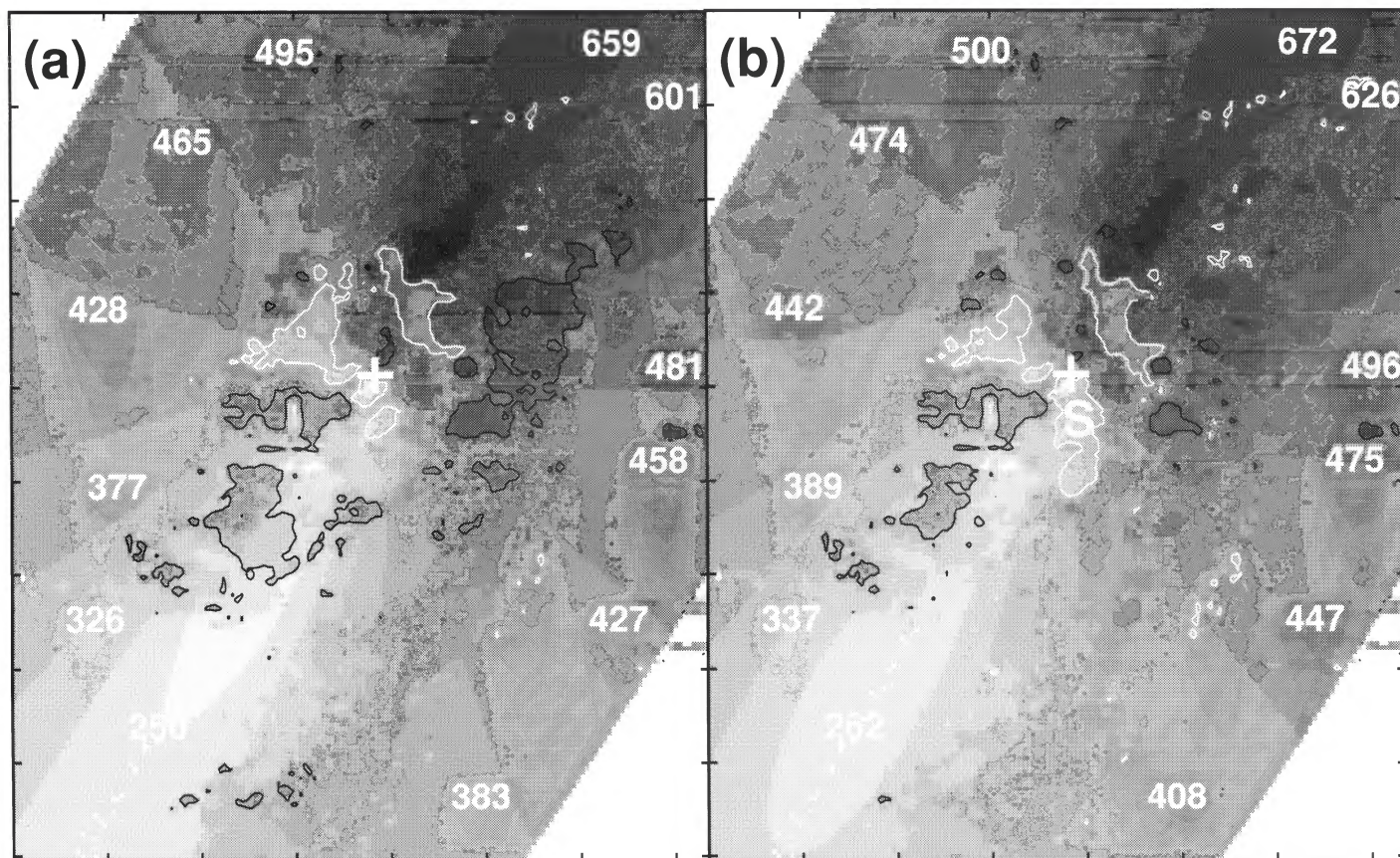
PLATE 3

FIG. 9.—Comparison of the observed Hα (from Fig. 2c) and model disk gas kinematics. In (a) and (b), the models were represented by the gray-scale "spider diagrams" that "underlie" the data (also plotted as a gray scale), and that deproject to a maximum radius of 17 kpc in the disk plane for a distance of 7 Mpc. Numbers are heliocentric radial velocities, ticks are drawn every 1.2 kpc (36″), the white plus sign marks the nucleus, and the "S" marks what is plausibly a shock associated with the bar. Residuals of (data − model) > 70 km s^{-1} are outlined in black (positive) and white (negative). Parameters for the axisymmetric disk (which rotates in a counterclockwise sense) are given in the text. (a) Model with circular gas orbits and $V_{helio} = 450$ km s^{-1}. (b) Model with bar forced, elliptical gas orbits (motions are summarized in Fig. 10), with $V_{helio} = 464$ km s^{-1}. The angle between the bar and the major axis in the plane of the disk is 74° (the bar major axis is at P.A. 17° on the sky). See also Figure 9c in text.

CECIL, WILSON, & TULLY (see 390, 369)

Huntley, & van Albada 1979) and so are not accounted for in our kinematic model. In support of the latter conjecture, we note that VA maps a sharp velocity gradient in H I at the same location, and that the region with deviant kinematics coincides with the dust lane and CO complex observed by PLRMN, as might be expected for a shock. The dust lane is easily seen in our $B - I$ color map (Fig. 8). The redshifted deviations E of the SE jet were noted by Rubin & Graham (1990), and attributed to a "drizzle" of gas raining onto the disk; we present a different interpretation in § 4.3. Deviations NW of the nucleus are discussed in § 3.3. These alternative explanations for the velocity residuals are unsatisfactory, but currently available data do not clearly discriminate between them.

While our exploratory kinematic models provide only limited guidance on how to distribute velocity deviations between jet and bar, Figure 10 shows that the bar is probably responsible for radial motions on the major axis at most ≈ 25 km s^{-1} in the disk plane near the jets. Our preferred tangential velocity curve lies within the envelope of H I velocities plotted by VA as his rotation curve number 2, despite our shift in the systemic velocity (Fig. 10). The velocity centroids of the emission-line profiles along both jets are within 60 km s^{-1} of the ambient disk motion.

3.2. The Helical Velocity Structure of the SE Jet

Figures 2d and 4 show that the velocity dispersion along the SE jet averages ≈ 80 km s^{-1} (corrected in quadrature for instrumental resolution), considerably above that in the H II regions (≈ 40 km s^{-1}). The dispersion of [N II] $\lambda 6583$ is systematically larger than that of Hα by about 13 km s^{-1} in the H II regions, perhaps because high-velocity gas with high [N II] $\lambda 6583$/Hα flux ratio is projected onto the H II regions along the line of sight. In the SE jet, where the [N II] $\lambda 6583$/Hα flux ratio is > 0.5, the velocity dispersions are very similar.

The Hα image of Ford et al. (1986) shows that the SE jet is actually resolved into several strands which appear to wrap

around each other ("braid"). We find that the large dispersions along this jet result from a regular kinematic braiding (see Fig. 7), with double-peaked Hα and [N II] $\lambda 6583$ emission-line profiles. There are also broad lines *near* the jet, but any discrete components are sufficiently blended that the line profiles can be fitted with single Gaussians. The braid pattern is indistinct in the velocity integrated flux map (Fig. 2a) because the strands are of comparatively low constrast and project into many of the monochromatic images, which have been summed. However, when our three monochromatic Hα images with the most obvious helical structure are summed after continuum subtraction (Fig. 11a [Pl. 4]), the pattern is striking at radii > 35" (where the widths of the line cores are small), and can be further accentuated by high-pass spatial filtering (Fig. 11c). Our images suggest that the strands are barely resolved laterally, with widths $\approx 2"$ (70 pc, corrected for seeing).

As we show in § 3.2.1, kinematic patterns are continuous in this region to smaller radii, where the *spatial* braiding is indistinct. All strands that can be seen in Figures 11a and 11c show the same sense of helicity and less than a twofold variation in pitch angle with increasing nuclear distance. The sense of helicity seems to reverse when velocity slices redward of those shown in Figures 11a and 11c are summed, although the pattern is less distinct because the signal-to-noise ratio is lower. Figure 11b summarizes the *kinematic* behavior at smaller radii, through simulations of long-slit spectra along and parallel to the SE jet, and shows that the velocity range decreases beyond 40" (1.3 kpc) radius. Nevertheless, the line widths at zero intensity remain large (≈ 500 km s^{-1}) beyond this radius. The simulated spectrum along the jet agrees well with Rubin & Graham's (1990) long-slit spectrum in P.A. 150°.

Figure 12 is a series of six space-velocity diagrams in which the loci of peak Hα emission in the broadest profiles are shown along the same "long slit" locations as simulated in Figure 11b. Close study of the midaxis profile shows that the peak emission at almost all locations may represent gas in three
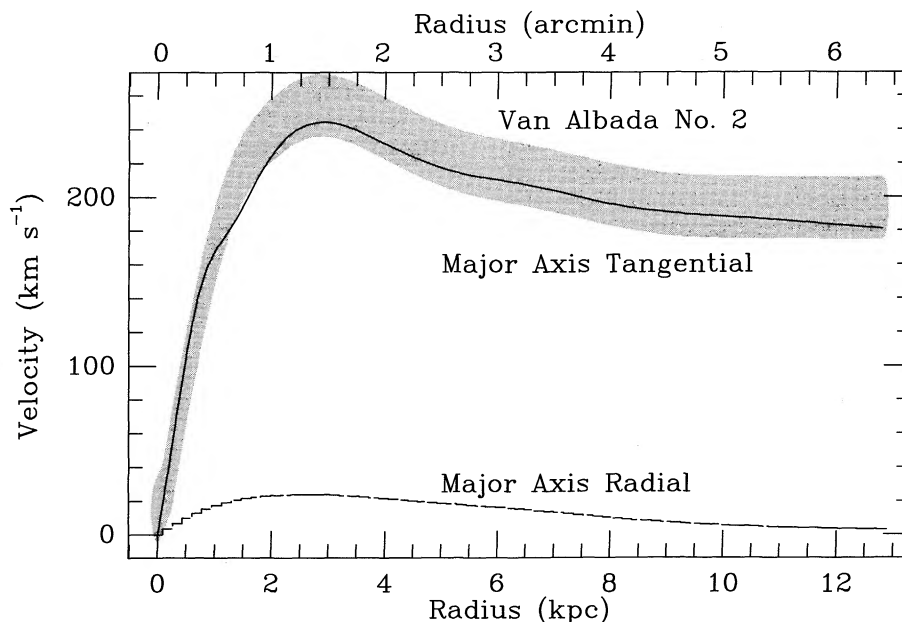

FIG. 10.—The gray band shows the range of rotation curves consistent with the H I $\lambda 21$ cm maps of VA. Also shown are the tangential and radial components along the major axis (P.A. 150°) that result from the elliptical orbits of our bar model. The tangential curve is consistent with the H I and the radial, bar-forced motions never exceed 25 km s^{-1}.
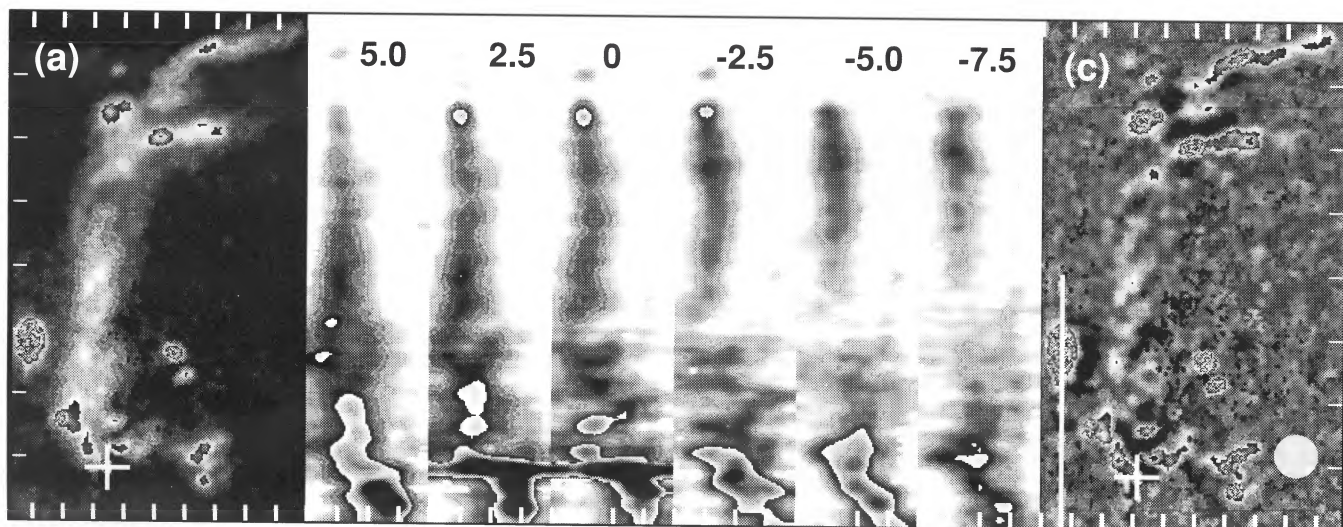
PLATE 4

FIG. 11.—(a) An image of the SE jet, formed by summing three monochromatic Hα images that straddle systemic velocity and with total velocity width 100 km s⁻¹. The figure has been rotated from the cardinal orientation so that P.A. 150° is vertical and runs from bottom to top. Vertical ticks are at 18″ (620 pc) intervals and horizontal ticks at 8″.5 (300 pc) intervals. The nucleus is at the plus sign. The flux distribution is seen to be composed of distinct helical strands. (b) Simulations of long-slit spectra along and parallel to the SE jet in P.A. 150° (the jet axis). SE is at top and NW at the bottom. Each panel covers 715 km s⁻¹ horizontally and the same spatial extent vertically as (a). The "slit width" is 2″.5, and each of the six panels is labeled by the midpoint (towards P.A. 240°) in arcseconds relative to the midaxis of the SE jet. Lowest velocities are left in each panel, and ticks along the horizontal axis are at 175 km s⁻¹ intervals, with systemic velocity at the middle tick. (c) The difference map: panel (a) minus panel (b) smoothed with the uniform circular kernal of 12″ diameter (shown). The white vertical bar shows the total distance in P.A. 150° plotted in Fig. 12.
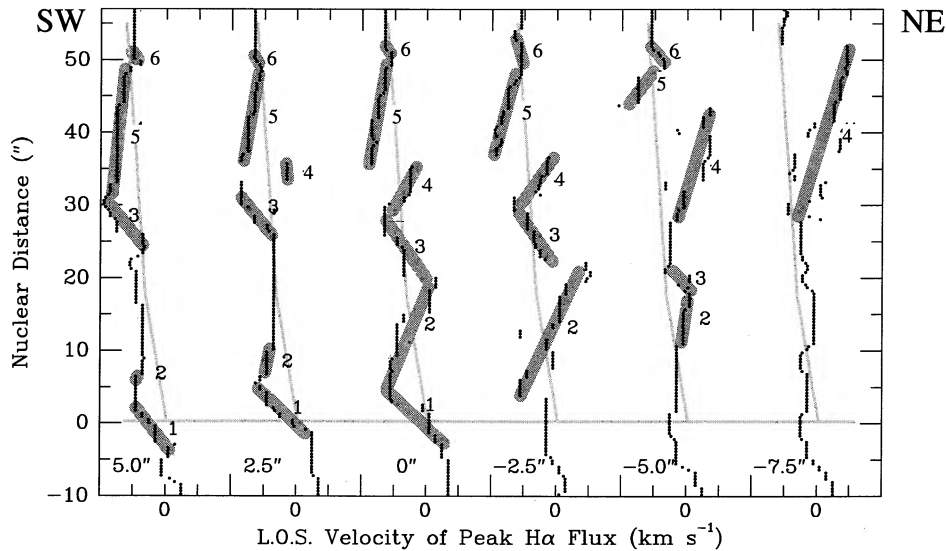
CECIL, WILSON, & TULLY (see 390, 370)

FIG. 12.—Six space-velocity diagrams in which the loci of peak Hα emission (*black vertical line segments*) in the SE jet are shown along P.A. 150° (vertical axis) in boxes 2″5 wide. The displacement (in arcseconds, toward P.A. 240°) of each diagram from the jet's center is indicated near the bottom. Velocities increase to the right and are relative to the heliocentric systemic velocity of 464 km s^{-1}. The ticks along the horizontal axis are separated by 175 km s^{-1}. The maximum radial extent of the gas in the extreme NE spectrum (-7″5 diagram) is uncertain because the highly redshifted gas blends with an incompletely subtracted night sky line. The thick gray diagonal lines represent the emission from each "braid," with the sequence 1–6 possibly representing distinct kinetic features (see text). The thin gray diagonal lines show the estimated ambient disk rotation. The horizontal dashed line shows the position closest to the nucleus in each diagram.

kinematic features, numbered 2, 4, and 5, that seem to start near the nucleus at blueshifted velocities and range over 400 km s^{-1} to the red. The line of sight velocities change sign across the jet midaxis, so that predominantly blueshifted gas is found to the SW, and redshifted gas to the NE, of the midaxis. Figure 11*b* shows a "bowing" of the midaxis long slit spectrum between 45″ and 90″ radius. The braid pattern breaks down beyond 75″ (2.6 kpc) radius, where the individual strands "open out" to form the three prominent branches at the end of the optical jet (Figs. 11*a* and 11*c*). We find no measurable kinematic deviation at the end of any of these branches, despite the large deflection angles on the sky.

3.2.1. *Decomposition of the Braided Emission-Line Profiles*

Our slit spectrum close to the midaxis of the braid pattern clarifies the structure of the rest of the Hα profile because it has higher signal-to-noise ratio than spectra in the HIFI data cube. Figure 7 shows that these profiles are clearly split into two velocity components, with separations up to 330 km s^{-1}, at many locations along the slit. To decompose each composite spectral profile, we assume that the velocity dispersions of the two components are the same, that their profiles can be approximated by Gaussians, that the continuum is adequately accounted for with linear ramps, that the [S II] $\lambda6717/\lambda6731$ ratio could not be smaller than its low-density limit, and that the velocity centroids of the two components of the [S II] and [N II] doublets and the Hα line are identical. The small residuals of the [S II] fits (Fig. 13) show that these are reasonable assumptions at most locations. The [S II] fits provide the best constraints because the blend is better defined for this doublet (when its ratio is at the low-density limit) than is the case for the excitation-dependent [N II] $\lambda\lambda6548$, $6583+$Hα complex.

Our decomposition shows that the [S II] doublet is indeed at its low-density limit (≤ 150 cm^{-3}), except at obvious localized H II regions (e.g., region D of MRNL), where [N II]

$\lambda6583/$Hα < 0.4, and at the nucleus. In these locations, we find maximum gas densities of ≈ 300 cm^{-3} and >1200 cm^{-3}, respectively. The internal velocity dispersion of each com-

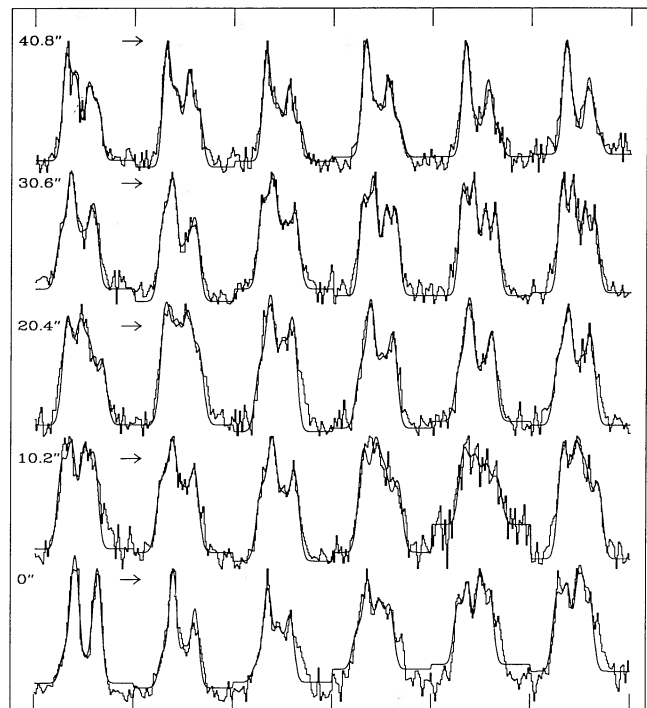

FIG. 13.—Normalized [S II] $\lambda\lambda6717$, 6731 doublet profiles and Gaussian fits to these profiles at each location along the slit in the SE jet, assuming a linearly sloping continuum (see text). The fitted continuum level has been overestimated at a few locations near the nucleus. Spectra are extracted from boxes 1″5 across and 0″85 along the slit at increments of 1″7, starting at the nucleus (*bottom left-hand corner*) and extending to 49″ radius (*top right-hand corner*). The arrows give the direction of increasing distance from the nucleus in each row. The range of wavelengths plotted is $\lambda\lambda6708$–6770.

ponent in the profile decomposition is ≈ 100 km s^{-1} (corrected in quadrature for instrumental resolution).

Figure 13 shows that the nuclear profile is broad and, compared with a single Gaussian profile, has enhanced flux on its blue wing. This is a common feature in the nuclear spectra of activity galaxies (e.g., Wilson & Heckman 1985). Our decomposition shows that this asymmetry is simply the extension of one of the kinematic subsystems to unresolved radii, an observation that may have significance for other active systems. The Hα profile has an additional broad component (Stauffer 1982; Filippenko & Sargent 1985).

Figure 14a plots kinematic parameters from the decomposition. From the nucleus to $\approx 3''$ radius we see a pair of distinct kinematic features, each of which shifts from red to blue velocities with increasing nuclear distance. From this point until $22''$ radius (definitely) or $\approx 30''$ radius (probably) we see another pair that moves from blue to red with increasing distance and have an approximately constant velocity gradient of 0.5 km s^{-1} pc^{-1}. At $22''$ radius the red component of the pair fades as a new, bright component enters the blue wing of the profiles. However, the faint red component still appears as a bump on the profile wing out to $\approx 30''$ radius. From $22''$ to $50''$, the brightest component shifts from -100 km s^{-1} to >200 km s^{-1}. An important constraint from our decomposition is that *two velocity systems with separations 300 ± 30 km s^{-1} are present in the profile near the midaxis, and that this separation remains roughly constant even though the absolute velocities of the two systems change substantially with distance from the nucleus.* Figures 14b–14d show radial Hα and [S II] intensity profiles of the brightest two components and their [N II] $\lambda6583$/Hα ratios. The [N II] $\lambda6583$/Hα ratio is systematically higher by ≈ 0.15 in the red component than the blue. On

average over all emission lines, the red component is $\approx 30\%$ brighter than the blue, perhaps because it is generated in denser media closer to the disk plane.

The picture is then of three features with only the central kinematic component (see Fig. 14a) being observed over a substantial fraction of a full cycle. The other two are seen over only a limited range of velocity before they leave the slit. The patterns discussed above are also evident in the "long-slits" derived from the Fabry-Perot data (Figs. 11b and 12). However, because of the lower signal-to-noise ratio of these latter data and their more limited velocity coverage, the picture here is somewhat confused by strands that shift from red to blue (features 1, 3, and 6 in Fig. 12) in antiphase with the brighter components. This is most apparent near $22''$ radius where, as the $2''.5$-offset spectrum (Fig. 11b) shows, the centroids vary rapidly from red to blue in the blended profiles. Figure 15c summarizes the possible structure of the SE jet derived from the analysis of the spatio-kinematic patterns in Figure 11.

3.2.2. Kinematic Models of the Helical Braids

We begin by noting that the mean velocity along the midline of the SE jet tends to track that of the adjacent disk (Fig. 12) and that the jet projects along the disk major axis (P.A. $\approx 150°$). For these reasons and others (e.g., MRNL), we shall assume that the jet lies close to the disk plane (at least in its inner regions, where optical line emission is seen) and hence lies close to the plane of the sky.

As shown above, both our images and velocity measurements reveal a "braided," presumably helical, structure for the SE jet. Two kinds of motion can lead to such a structure: (a) pure ballistic outflow of the gaseous elements, with the sources
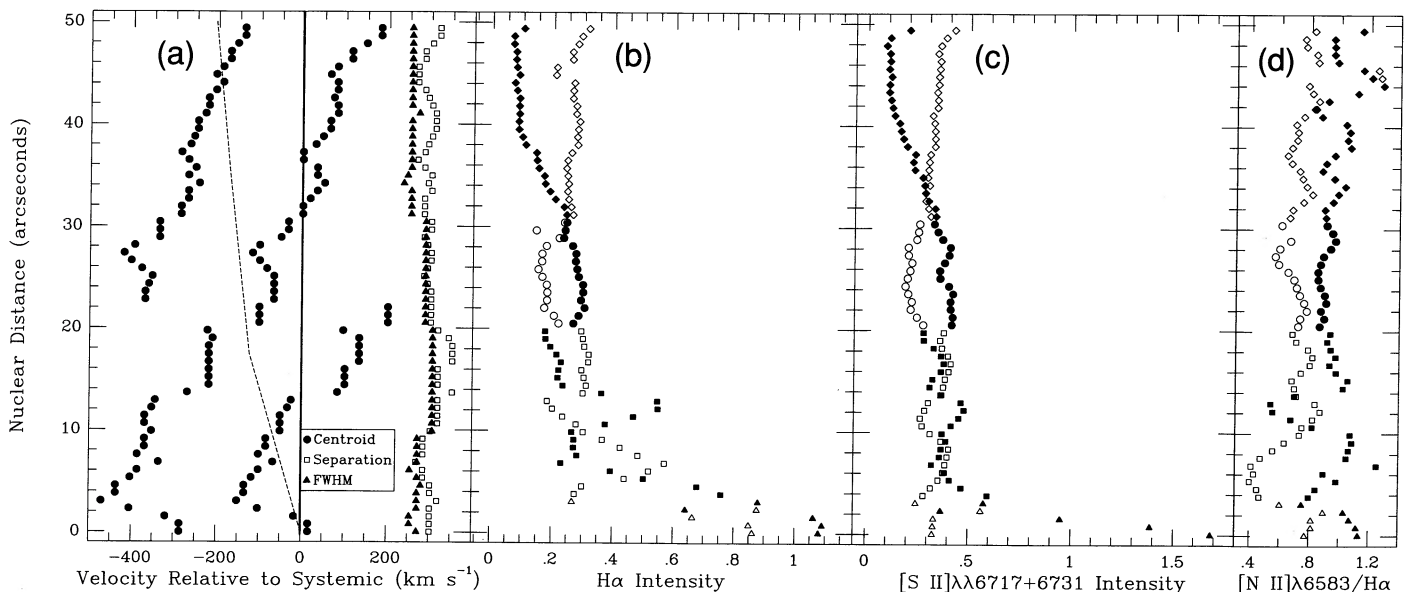

FIG. 14.—Kinematic (a), line intensity (b) and (c), and line intensity ratio (d) parameters derived from the decomposition of each emission line into two Gaussian components in the long-slit spectrum near the midaxis of the braid pattern in the SE jet at P.A. 150°. (a) The velocity centroids (relative to the systemic velocity of the galaxy) of the two brightest components at each location along the slit are shown as filled circles, together with their velocity separation, and FWHM (assumed equal, see text). Although only two components are plotted at each radius, a third is often detected as residual flux on the red wing. The slanted long-dashed line approximates the estimated ambient disk rotation near the SE jet, and the vertical dashed line is at the systemic velocity. (b)–(d) Intensity and intensity ratios of different species along the SE jet. All intensities are in the same arbitrary units. The two kinematic components were separated by constrained Gaussian fits (see text). The "red" component is plotted with filled symbols and the "blue" with open symbols, for the following sections labeled in Fig. 12: filled and open triangles (1); filled and open squares (2); filled and open circles (3), and filled diamonds (4) and open diamonds (5).

of the braided strands oscillating or orbiting about one another, and (b) real helical motion in which the gas is continuously forced to follow spiral trajectories. Because we have measured *both* the spatial *and* the velocity structure of the jet, we can apply three simple kinematic tests in an attempt to distinguish between (a) and (b).

1. Along the center line of the jet, the velocity pattern ("long-slit image") should be 90° out of phase with the image pattern for pure ballistic motion, but in phase with it for real helical motion. Although the spatial braiding is hard to trace at small radii, Figures 15a and 15b (Plate 5) suggest in-phase spatial and velocity braiding, favoring helical motion.

2. If the far side of the pattern is preferentially attenuated by dust, then the mean velocity centroid of the pattern along the center line should be preferentially blueshifted with respect to adjacent gas for pure ballistic motion, but is expected to be equal to that of adjacent, ambient gas for real helical motion. In fact, Figure 14a shows that the braid pattern is found at both lower and higher velocities than the local rotation curve, but is preferentially blueshifted with respect to the systemic velocity, so this test is inconclusive.

3. For pure ballistic motion with mean direction close to the sky plane, the mean velocity will roughly equal that of adjacent ambient gas at the "left" or "right" edges of the pattern. On the other hand, for real helical motion, the mean velocity will be blueshifted (redshifted) with respect to the ambient velocity at the "left" ("right") edges of the pattern. This last pattern is, of course, reversed for an opposite sense of winding of the helices. Figure 12 shows the pattern expected for motion with a substantial helical component.

On balance, these results suggest significant helical motion rather than pure ballistic outflow. In detail, however, the interpretation is complicated by our limited spatial and spectral resolution of individual strands and their significant internal velocity dispersions. Therefore, we simulated long-slit spectra across a conical braided structure (Fig. 16 [Pl. 6]). For simplicity our models assume that the axis of the braid pattern is linear, although radio data with 6″.5 FWHM (van Albada & van der Hulst 1982) suggest that the active flow may twist through about 30° in projection from the nucleus to 40″ radius. A concern for any model with substantial ballistic outflow from the nucleus is that the full opening angle of the SE jet pattern is <15° in the braided region, so the 640 km s^{-1} velocity range that is observed along the cone's midaxis (Fig. 14a) would correspond to a true outflow velocity of >2000 km s^{-1}. Such large velocities seem rather implausible to us, because they exceed the observed line widths. However, they have independently arisen in previous dynamical models of the anomalous arms, in which an instantaneous expulsion of gas from the nucleus, rather than the currently favored jet, was postulated (van der Kruit, Oort, & Mathewson 1972; van Albada 1978). These large outflow velocities are not implied when the motion is truely helical, because the helices twist through large angles both on the sky and with respect to our line of sight. In considering these models, an important caveat is that our emission-line velocities may not reflect the true outflow velocities, but may rather correspond to high-density, ambient clouds in a sheath around, and excited by, a fast, low density, jet. Thus, our observed velocities may bear only an indirect resemblance to these empirical models.

Parameter values were chosen by experiment to reproduce the observed brightness distribution in Figure 11a. The main geometric constraint is provided by the shape of the braids near the pattern boundaries at nuclear distances of >40″. This observation shows that the axis of the braid pattern must be tilted by <30° to the sky plane, to prevent the braids from "piling up" along the line of sight. This is a loose constraint from an idealized geometry because the strands are breaking out of their braid pattern at these large nuclear distances. The *paired* velocities at smaller radii from our decomposition near the braid midaxis suggest that the strands overlap in projection, so that the repeating velocity gradients arise from tight curvature of an intertwined, optically thin braid pattern. We estimate from the relative brightness of the two kinematic components in our decomposition that any extra attenuation of the backside component corresponds to at most $A_V = 1.5$ mag. If the attenuation is higher, the strand behind disappears and double profiles are not produced.

Three strands are visible at large radii (Figs. 11a and 15). Experiments showed that profiles with constant velocity separation between the two prominent components could not be produced at small radii with only two strands, for any attenuation distribution. Contrary to our previous report (Cecil 1991), the third strand therefore *does* appear to contribute to the line profiles in the near-nuclear region spanned by Figure 12. The marginally resolved strands show no indication of edge-brightening. We therefore simply parameterized their cross sectional brightness distribution as cos^n θ, where θ is the angle from the strand's axis, with θ varying from 0° at the middle of the stand to 90° at its edge. The models plotted in Figure 16 correspond to $n = 2$.

We first modeled the profiles that arise from gas flowing *along* the helices. Figure 16a shows that a helical flow naturally reproduces the bright, winding filament at nuclear distance ≈29″–22″ seen in the 0″ and 2″.5 spectra of Figure 11b, and the blueshifts and redshifts from the velocity of the ambient disk near the SW and NE boundaries of the braid pattern, respectively (Fig. 12). Figure 16b shows that a very similar pattern is produced by optically thin strands that are embedded in an attenuating medium. However, in neither case could we find a parameter set that simultaneously produced "long-slit" profiles with *constant* velocity separation between two peaks, as is observed (Fig. 14a).

Ballistic models (Fig. 16c and 16d), however, can reproduce profiles with constant velocity separation, and also the observed large gradients that alternate in sign near the midaxis of the pattern (Fig. 12). In summary, we are unable to completely exclude outflow with a substantial radial (ballistic) component, but believe that the current data argue that the dominant motion is along the helices.

3.3. *The Interaction between the NNW Jet and the Interstellar Medium*

MRNL show that the brightest Hα flux within 1.2 kpc radius is elongated and bounded by CO complexes. They suggest that the jet is confined to the narrow channel by molecular gas. Our Hα data show direct kinematic evidence for confinement, in that we find a stream of high-velocity gas between the CO complexes (Fig. 17 [Pl. 7]). In fact, the jet appears to "bounce" off the interstellar clouds at two or possibly three locations. The jet plausibly starts from the nucleus (Hα knot "a") along P.A. ≈ −5°, and first encounters CO cloud complex number 3 (CO No. 3) of PLRMN. This interaction, some effects of which are probably visible as Hα knot "b" in Figure 17b, deflects the jet toward P.A. ≈ −50°. Then it encounters another cloud that
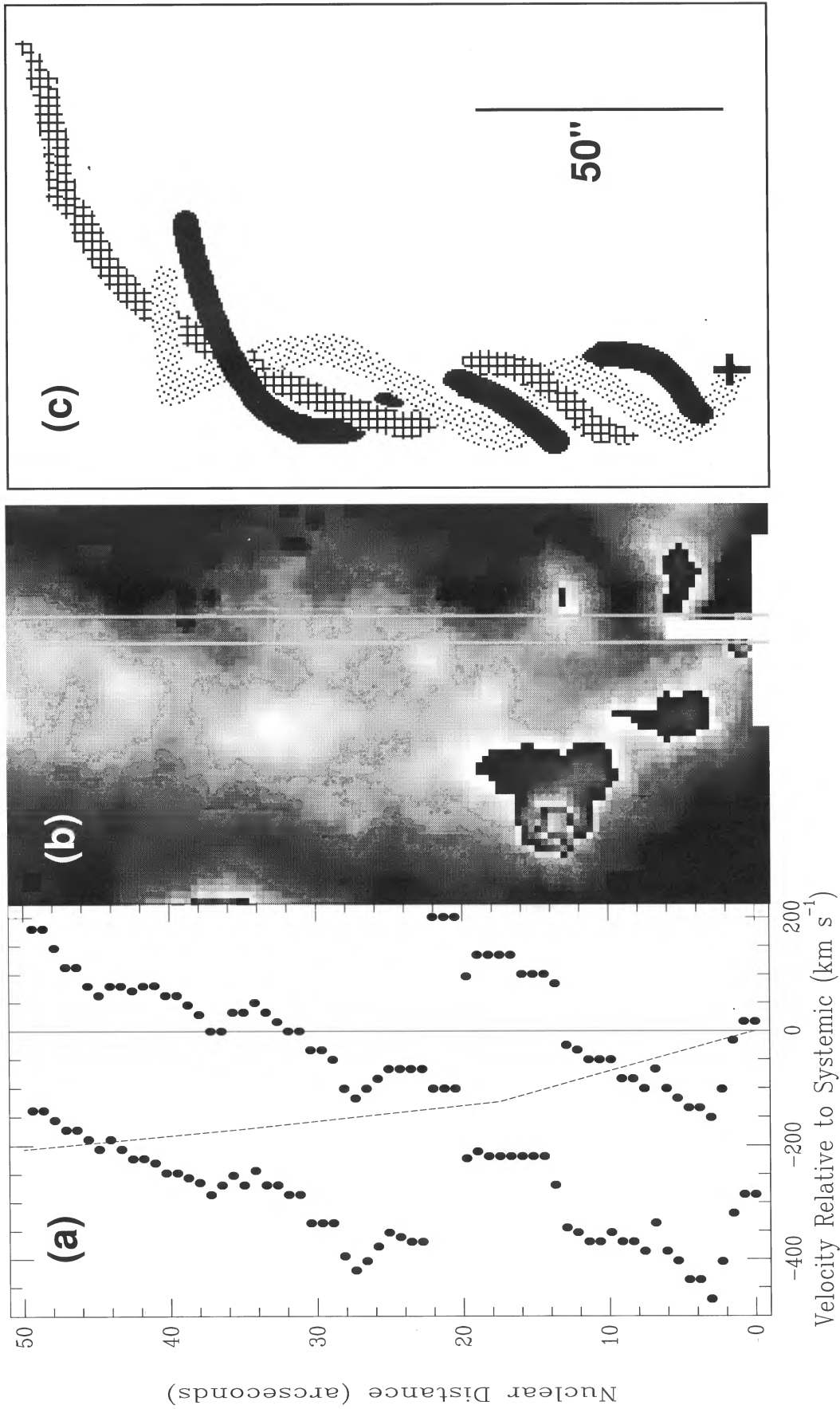
PLATE 5

FIG. 15.—Correlation of kinematic (a) and spatial (b) braiding at small radii SE of the nucleus, suggesting that the gas flows in an intrinsically helical path (see text). (b) is an enlargement of part of Fig. 11a showing the sum of three monochromatic Fabry-Perot images at velocities slightly blueshifted from systemic, while (a) comes from Figure 14a and shows the velocity centroids of the individual "braid" strands of the jet. Regions with high-velocity gas appear dark in (b). The vertical lines in (b) show the nominal location of the slit spectrum whose velocity content is parameterized in (a). Note that structure within 10″ radius is hard to interpret in panel (b) because of the large range in line-of-sight velocities in this inner region. (c) A schematic diagram of a possible spatial structure of the triple helix SE of the nucleus; we caution the reader as to the inherent ambiguity in the identification of different segments of any given strand, especially at radii <15″. The strands extend slightly beyond the ends shown here, with much fainter surface brightness. The vertical line shows the radial range plotted in (a) and (b).

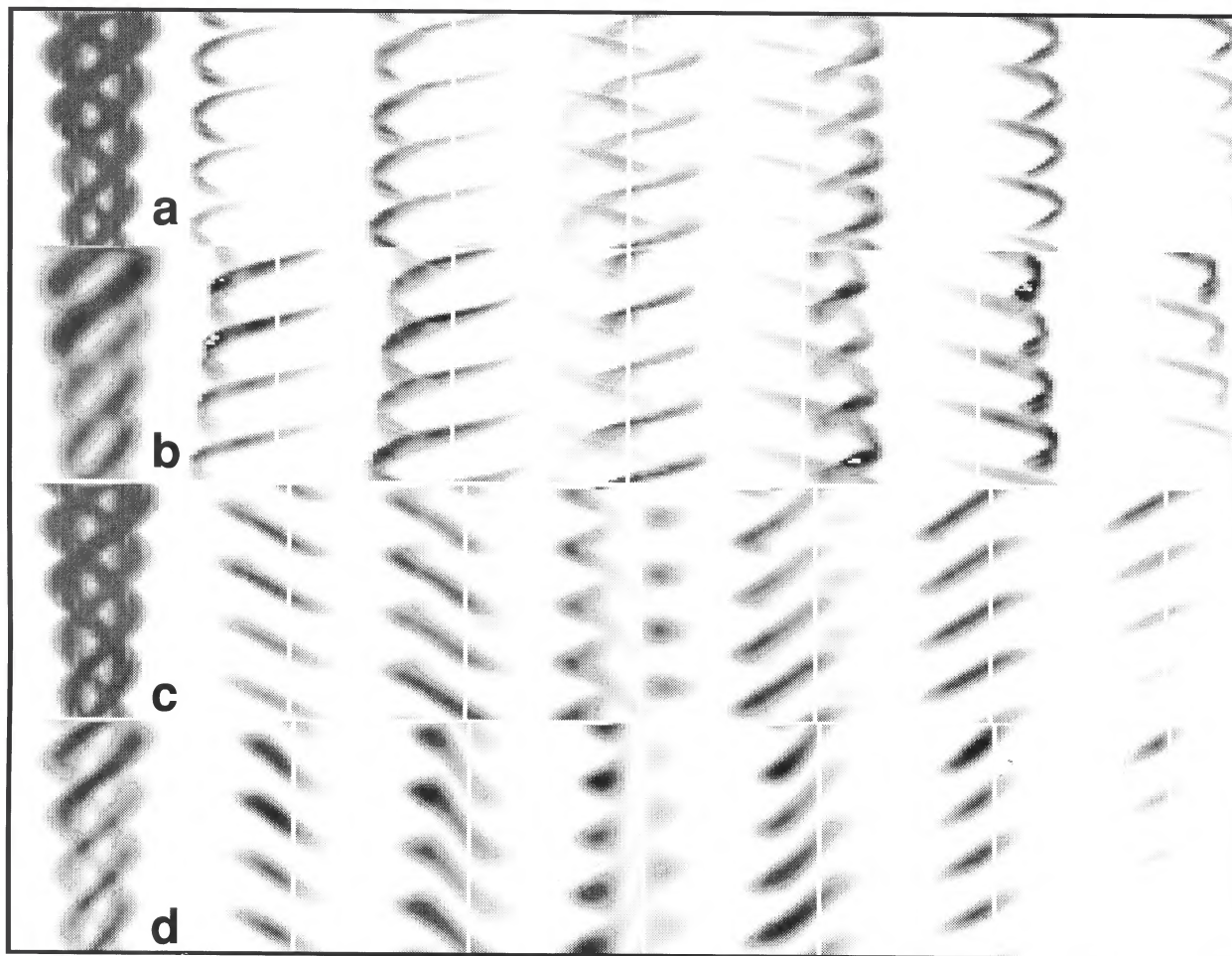CECIL, WILSON, & TULLY (see 390, 373)

PLATE 6

FIG. 16.—Models of the spatiokinematic structure of the inferred, triple helix SE of the nucleus, with various assumptions on the velocity field of the ionized gas. The projected spatial appearance of the model braid pattern is shown in the left panel of each row, with the edges of the long "slits" delineated by vertical white lines. The patterns have maximum width ≈18″ and are ≈50″ high. The nucleus is near the bottom of each panel. The axis of the braid pattern is tipped 2° toward the line of sight, and each strand has a cross sectional brightness distribution proportional to $\cos^2 \theta$ (i.e., center brightened, see text). The six panels on the right of each row are space-velocity plots (simulated long-slit spectra with "slits" 2″.5 wide) following the formats of Figs. 11b and 12; the vertical white line marks systemic velocity. In (a) and (c) the strands themselves contain partially opaque material, while in (b) and (d), this material is in the medium *between* the strands. (a) and (b): Motion along the helices. (c) and (d): Pure ballistic outflow ("garden hose" model).

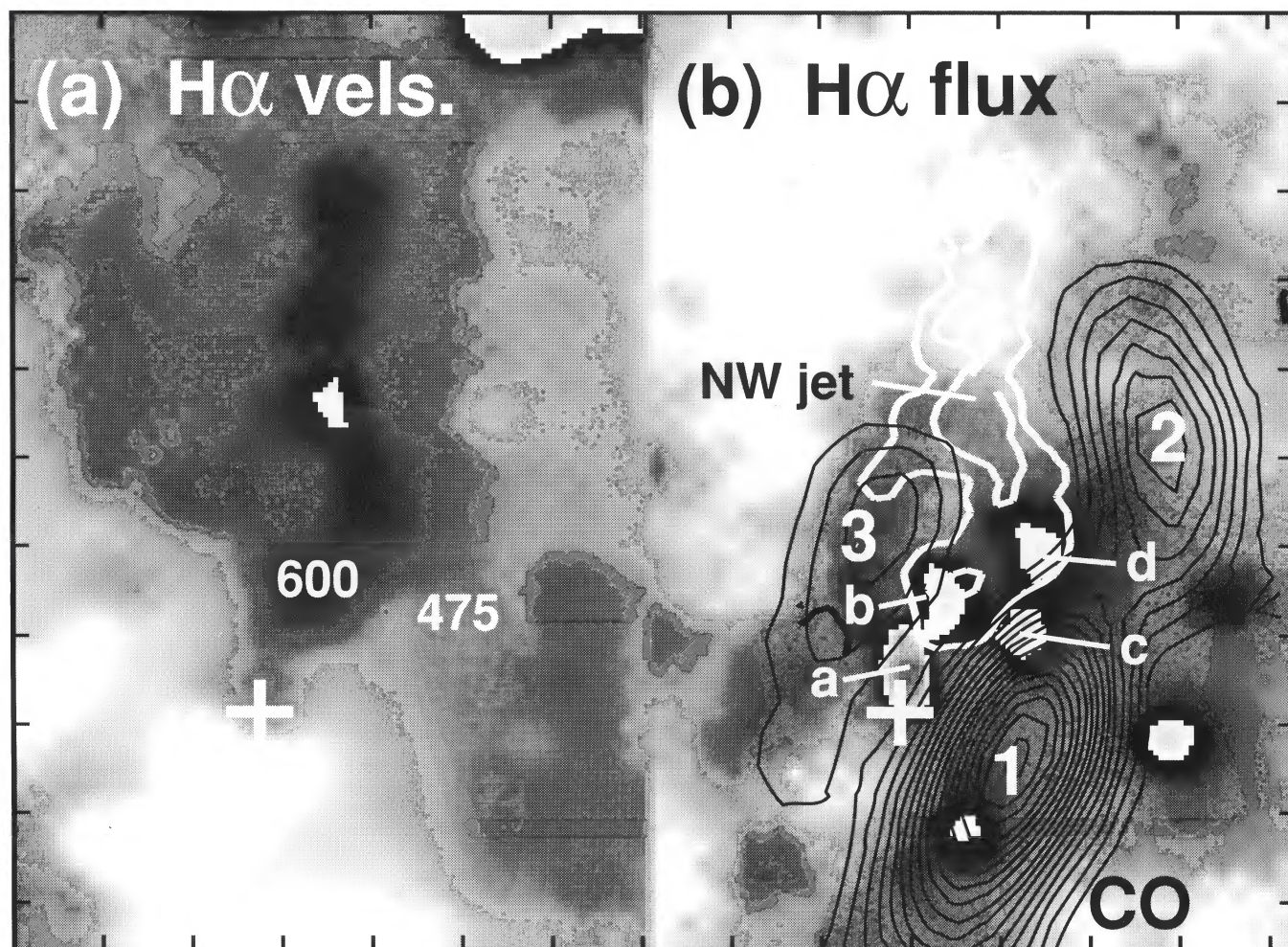CECIL, WILSON, & TULLY (see 390, 373)

PLATE 7

FIG. 17.—The interaction between the NNW jet and dense molecular cloud complexes. The nucleus is at the plus sign and the ticks are at 5″ intervals. (*a*) A gray-scale plot of the recession velocity of Hα, darker shades representing higher velocities. The shades representing 600 and 475 km s^{-1} are indicated. (*b*) A gray-scale plot of the Hα flux (shade is proportional to the square root of the flux), with the shade cycling from white (lowest flux) to black and back to white in the brightest knots. The black contours represent CO emission (from PLRMN), and the three CO clouds are numbered 1, 2 and 3 following the notation of PLRMN. The two white contours are drawn at Hα velocities of 550 and 625 km s^{-1}. The four bright knots (labelled [a]–[d]) in the Hα emission along the jet boundary are plausibly interactions between the jet and the interstellar medium.

CECIL, WILSON, & TULLY (see 390, 373)

redirects the flow along P.A. $\approx -8°$. This interaction, traced by Hα knots "c" and "d," may accelerate the deflecting cloud (component CO No. 2 of PLRMN) to a velocity of several hundred km s^{-1}, according to PLRMN. A third deflection, evident by the discontinuity in velocity toward the top of Figure 17a, is less well defined.

Figure 18 shows that the line-of-sight velocities along the NNW jet follow the disk rotation, but are systematically red-shifted by ≈ 80 km s^{-1}, on average, from those of the sur-rounding gas. The jet motion is apparently responsible for the abrupt velocity increase NNW of the nucleus along P.A. 150° at radii $< 12''$ that is plotted by Rubin & Graham (1990) and in our Figure 6. The velocity difference between the jet and the surrounding gas increases to 120 km s^{-1} when the jet bends away from this position angle $\approx 7''$ from the nucleus. The jet curvature here (Fig. 17) seems to arise from a true bend in the flow, so we may simply be seeing more of the outflow velocity projected along the line of sight. If the jet flow is directed along P.A. $\approx -50°$ here, the velocity difference between jet and sur-rounding gas deprojects to 140 km s^{-1} in the disk plane.

Our spectral fits isolate Hα emission from the local contin-uum more effectively than does the interference filter imaging of MRNL, and we find that the line of enhanced Hα flux within the channel breaks up into discrete knots. Four such knots (marked a–d in Fig. 17b) lie along the boundaries of the NNW jet as traced by its kinematic disturbance, at "elbows" where the jet locus bends. These localized brightenings correspond to
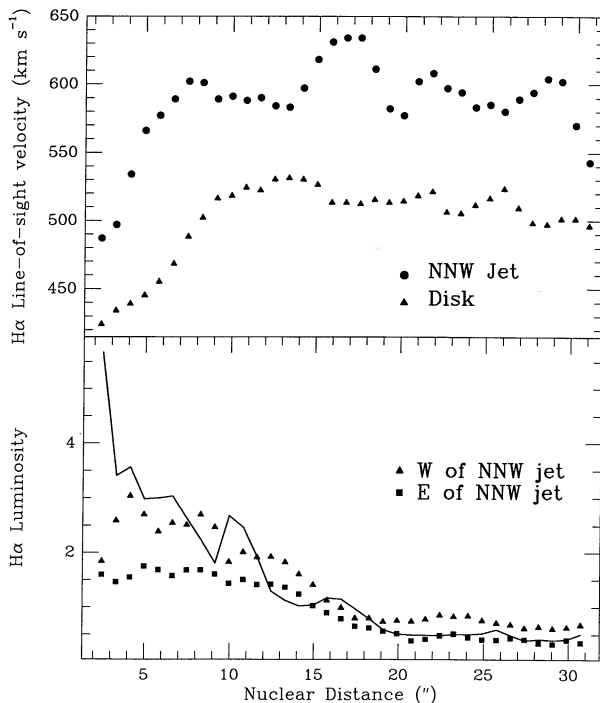
masses of (6, 2, 2, 3) $\times 10^4$ $M_{\odot}$ (1 cm$^{-3}/n_e$) for a, b, c, and d respectively. Similar brightening is seen at the boundaries of other bent jets and is often interpreted as emission from inter-nal shocks (Icke 1991). The ratio of the intensities of the sulphur doublet [S II] $\lambda\lambda6717$, 6731 shows that the gas in the NNW jet is at the low density limit ($n_e \leq 150$ cm^{-3}).

MRNL identified the NNW jet with a ridge of enhanced Hα emission $\approx 5''$ W of our kinematic disturbance. However, this ridge is actually the ionized E boundary of the extended CO complex (CO No. 1, 2; see Fig. 17b) whose discrepant kine-matics were discussed by PLRMN. Figure 18 shows that the jet becomes fainter than the ionized ridge beyond 18$''$ from the nucleus.

There is evidence for significant kinematic disturbances by the NNW jet at larger nuclear distances. Our profiles are ≈ 250 km s^{-1} (FWZI) broad near 73$''$ (2.5 kpc) from the nucleus along P.A. $-30°$, where Rubin & Graham (1990) find profiles spanning 500 km s^{-1} which they speculate are due to a "galactic chimney" (we attribute the difference in line width to the higher signal-to-noise ratio of Rubin & Graham's spectra.) In addition, there is a compact X-ray source nearby, with lumi-nosity $\approx 10^{39.7}$ ergs s^{-1} (for 7 Mpc distance) in the Einstein HRI bandpass (Fig. 2a). We note that the radio continuum maps of van Albada & van der Hulst (1982) and Hummel, Krause, & Lesch (1989) both show one branch of the NNW jet crossing this region, so it is plausible that we are seeing line emission from this jet branch, rather than from a localized "chimney."

4. DISCUSSION

Radio continuum maps show the full extent of the jets (van Albada & van der Hulst 1982). Van der Kruit et al. (1972) have developed a ballistic model for the jets and trailing radio "plateaus" that was subsequently refined by van Albada (1978). In this picture, $\approx 10^7$ $M_{\odot}$ of gas (KE $\approx 10^{56}$ ergs) was ejected from the nucleus $\approx 4 \times 10^7$ yr ago, in a single event with velocities 400–1500 km s^{-1} relative to the rotating ISM. The ejection direction was roughly E-W on the sky, and almost in the plane of the disk. The ejecta were supposed to be braked by the ISM and so acquired angular momenta. This braking twisted their loci through the observed radio plateaus into their present alignment along the leading edge of the plateaus, where they are expected to have mean motion at or less than the disk tangential velocity. The synchrotron emission was assumed to arise from compression of the ambient disk mag-netic field by shocks. Van der Kruit (1974) found that the Hα velocities along the anomalous arms are indeed reduced as the model predicted, and our data confirm this result. The relative faintness of emission-line compared to radio-continuum radiation in the plateaus plausibly arises from faster rates for atomic recombination than synchrotron cooling [10^5(1 cm$^{-3}/n_e$) vs. 10^7 yr. MRNL] in the disk ISM.

The intensity ratio of the sulphur doublet [S II] $\lambda\lambda6717$, 6731 is in the low-density limit ($n_e \leq 150$ cm^{-3}) along the jets (except at an obvious H II region near the end of the SE jet). The typical Hα brightness of the strands is 1 (1 cm$^{-3}/n_e$) $M_{\odot}$ pc^{-2} (Fig. 2a), which implies $n_e > 0.8$ cm^{-3} for our upper limit on the strand diameter of $2'' = 70$ pc.

4.1. X-Ray Emission from the SE Jet

The recently published Einstein HRI soft X-ray map of NGC 4258 (Fabbiano et al. 1991) provides an important new con-straint on this outflow. The contours, smoothed to $\sigma = 16''$,

FIG. 18.—(Top) Hα recession velocities plotted against nuclear distance for the NNW jet. The velocities were extracted from regions 3$''$.4 (120 pc) wide across the jet and centered on the peak kinematic disturbance. The average of the disk velocities on either side of the jet is also shown. The jet's velocity is seen to follow the disk rotation but is systematically redshifted by ≈ 80 km s^{-1} from its immediate surroundings. (Bottom) The solid line shows Hα surface luminosities in units of $M_{\odot}$ (1 cm$^{-3}/n_e$) pc^{-2} along the NNW jet with the same extraction limits as above. The jet becomes fainter than its surroundings (indicated by the filled square and triangles) beyond 18$''$ radius.

are plotted in Figure 2a. A compact X-ray source is centered in the crook of the NNW anomalous arm. However, the most luminous structure is resolved and coincides with the *optical* extent of the SE anomalous arm. The emission extends from the nucleus down the SE arm, peaking at 2.5, where the braid pattern breaks up and the jet strands turn through a large angle on the sky. Fabbiano et al. (1991) report an X-ray flux (integrated over the HRI passband) of 3.7×10^{-12} ergs cm^{-2} from the SE feature. Approximately 75% of this flux coincides with the braided SE jet, so we take the X-ray luminosity of the SE jet as 1.8×10^{40} ergs s^{-1} for our adopted distance of 7 Mpc.

To establish the volume emissivity, we estimate the volume of the braided jet to be (2.5 kpc) $\times$ (3 braids) $\times \pi \times$ (35 pc)$^2 \times$ (1.5) = 1.2×10^{63} cm$^3 = V_{63.1}$ (the factor of 1.5 approximates the increase in arc length due to the helical structure). If we assume that the X-ray flux comes from hot, shocked jet gas that emits thermal bremsstrahlung, we obtain (e.g., Rybicki & Lightman 1979) for the volume-averaged emissivity

$$1.5 \times 10^{-23}/V_{63.1} = 1.4 \times 10^{-27}T^{1/2}n_e^2 Z^2\overline{gB} \text{ ergs s}^{-1}\text{ cm}^{-3},$$

where the charge Z and effective Gaunt factor $\overline{gB}$ are both ≈ 1.2. Therefore, $T^{1/2}n_e^2 \simeq 6200/V_{63.1}$, so if $T \approx 10^7$ K, the average number density of the hot gas is $2/(V_{63.1})^{1/2}$ cm^{-3}. Bremsstrahlung would then be the dominant form of cooling, with time scale $t_{br} \simeq 2000T^{1/2}/n_e \simeq 3 \times 10^6$ yr. Shock velocities of ≈ 560 km s^{-1} would be required to generate gas at this temperature, and might arise as disk gas is entrained into the jet. The mass of hot gas would be $2 \times 10^6(V_{63.1})^{1/2}$ $M_\odot$. Further investigations of the X-ray emission, at both higher spatial and spectral resolutions, are needed to determine the emission mechanism of the X-rays and to explore the relationship of this component to the optical line emission.

4.2. Consequences of Jet Flow Near the Disk of NGC 4258

The current interpretation of the anomalous arms is that first provided by Ford et al (1986), based on their Hα images, and augmented by the images and CO velocities of MRNL. In this picture, a jet bores a tunnel through the galaxy ISM. A jet substantially reduces the required energetics of the outflow because subsequent ejecta can travel down this largely evacuated tunnel through the rigidly rotating inner disk. Eventually, the rotation curve turns over, the active tunnel is sheared, and the now fossilized jet trails the disk as it fades. Subsequently, the jet reaches larger radii along a new tunnel. Our data agree with this interpretation of the anomalous arms as jets in rough pressure equilibrium in the dense disk. MRNL suggest that this picture is supported by the apparent bifurcation of the two jets at similar galactic radii on both sides of the nucleus. Anomalous gas motions (§ 3.3 and Rubin & Graham 1990) and the radio map of van Albada & van der Hulst (1982) suggest a third strand in the NNW jet that splits off at $\approx 30''$ radius; the SE jet also has three prominent strands. Our data contradict the suggestion of MNRL that the N and S strands at the tips of the NNW and SE jets, respectively, are the youngest. Instead, we find that the SE jet is already split into three components with similar kinematics and line fluxes at similar distances from the nucleus, and only the *braids* separate at large radii (Fig. 15).

As a general consideration for a kinematic model with appreciable nuclear outflow, any tilt of the axis of the SE braid pattern out of the plane of the sky must be $\lesssim 10°$, so that the velocity centroid tracks the ambient disk rotation (Fig. 12).

Note that this also places the braid axis close to the plane of the disk. The ballistic model of Van der Kruit et al. (1972) also requires ejection near the disk plane.

In the less favored ballistic interpretation of the kinematics (§§ 3.2 and 4.4.1), motions at small radii are consistent with an ongoing outflow in all three strands at a single velocity of $\approx 2 \times 10^3$ km s^{-1}. Even if the motion is instead along the helices, the outflow velocity cannot be very much smaller than this number, because the anomalous arms must presumably be generated in a fraction of the orbital period of the inner disk. If the helical motion is along twisted magnetic flux tubes, the synchrotron-emitting jet may also be braided. The radio observations of NGC 4258 with the highest spatial resolution (6".5 FWHM; van Albada & van der Hulst 1982) separate the anomalous arms into filaments, but the resolution is inadequate to see braids, let alone resolve their widths.

4.3. Gas in the Radio Plateaus

Rubin & Graham (1990) have found kinematically disturbed ionized gas (which they term "drizzle") in the radio plateaus. The most prominent disturbance lies along the SE braided jets. Our more extensive Fabry-Perot spectra confirm their observations, and reveal that the complex line structure and broadening along these jets arise directly from the helical braiding. Relatively strong emission from night sky lines prevented us from synthesizing spectra in the radio plateaus. However, Figure 19 (Plate 8) shows two Hα images of the SE quadrant of the galaxy, both derived from the Fabry-Perot data cube. These images show gas between -130 and -25 km s^{-1} (a) and between $+120$ and $+190$ km s^{-1} (b) with respect to systemic velocity. Figure 19b reveals an extensive network of gaseous filaments in the region upstream of the SE jet, within the SE radio plateau. These filaments are wider and more diffuse than the braids of the jet itself and are presumably related to the "feathery" emission-line profiles found in this region by Rubin & Graham (1990). Although the nature of this gas is unclear, it tends to be redshifted with respect to systemic (cf. Fig. 11). The filamentary structure is suggestive of old, relaxed braids. An ad hoc explanation for this high-velocity gas and the radio synchrotron emission in the plateaus is that the jet axis has precessed to its present alignment in P.A. 150° from an approximate E-W alignment. Both the emission-line and radio-emitting gases would then be tracers of past activity in the nucleus of NGC 4258. VLBA radio observations of the nucleus may be able to confirm the present orientation of the source of the jets.

4.4. What Braids the SE Jet?

The variations of the emission-line profiles along the SE jet may be accounted for by three intertwined, helical streams. MRNL attributed the splitting of the strands at the end of the SE jet to an intermittence of $\approx 10^6$ yr between ejections. However, the continuous kinematic patterns argue that the time scale associated with any intermittence in the outflow is substantially longer than the braid cycle time.

4.4.1. Ballistic Ejection from Nuclear Sources

One possible braiding mechanism is ballistic ejection from orbiting compact sources. Figure 12 shows that the innermost braids have similar pitch angles and wavelength ≈ 1.4 kpc. If the outflow speed deprojects to $\approx 2 \times 10^3$ km s^{-1}, as suggested by our upper limit on the local opening angle, we derive an orbital period $P_{Myr} = 0.6$. If the observed velocity range of 640
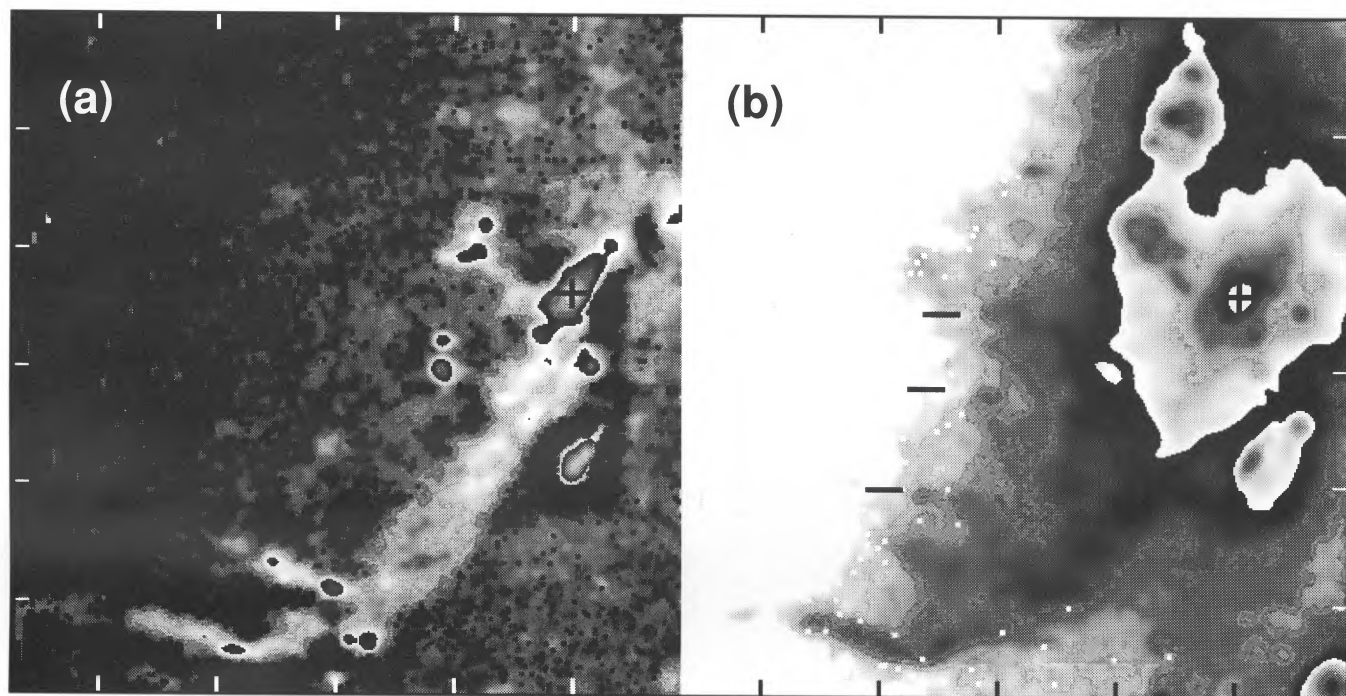
PLATE 8

FIG. 19.—Log-scaled images of the Hα flux distributions at different velocities SE of the nucleus. The gray-scale shade cycles back through black in the brightest regions. Ticks are at 1 kpc (28″) increments, with N at top and E at left. The nucleus is indicated with a plus sign. (a) The image formed by first summing the three images with velocities relative to galaxy systemic between −130 and −25 km s⁻¹, then smoothing the result by a Gaussian with a circular kernel of 20 pixels (17″), and finally subtracting the smoothed image from the unsmoothed sum to remove slowly varying structure. This procedure accentuates the braided jet. The faint, concentric rings of emission arise from variations in the night sky intensity in the original frames. The linear gray scale cycles from white back to black in the brightest regions. (b) The image formed by summing the three images with velocities relative to galaxy systemic between +120 and +190 km s⁻¹. Hα filaments are apparent *throughout* the SE plateau, not just along the edge with the braided jet. Prominent filaments not present in (a) are marked. The inverted gray scale is linearly scaled in faint regions and logarithmically scaled near the nucleus (where intensities cycle from black to white).

CECIL, WILSON, & TULLY (see 390, 375)

km s^{-1} along the midaxis of the braid pattern (Fig. 14a) is interpreted as an orbital motion of ≈ 320 km s^{-1}, the sources are separated by 6 pc (maximum separation 0″.2 on the sky). The combined mass is $M_{tot} = 9 \times 10^3 d_{pc}^3 / P_{Myr}^2$ $M_\odot$, where d_{pc} is the orbit diameter in parsecs. The braids are interleaved with similar transverse amplitude of ≈ 320 km s^{-1}, so it is plausible that each source has a similar mass of $\approx 3 \times 10^6$ $M_\odot$.

Such compact, supermassive objects are presumably black holes. Begelman, Blandford, & Rees (1980) have considered the dynamical evolution of a supermassive black hole binary, formed through the merging of two galactic nuclei. The evolution proceeds through several stages: any associated stellar clusters merge, the holes sink to the center of the stellar distribution and then become bound to each other, dynamical friction causes the holes to spiral together until the binary becomes sufficiently tightly bound that gravitational radiation rapidly shrinks the orbit, and finally the holes coalesce. The parameters derived above suggest that the orbital period has approached or exceeded the stellar velocity dispersion, so that the binary is now "hard." Evolution to this stage would have proceeded via dynamical friction with stars and the abundant ($\approx 2 \times 10^8$ $M_\odot$ for CO complex No. 1 of PLRMN) molecular gas in the inner several hundred pc. If the rotation axes of the black holes are misaligned, the spin axes will undergo geodetic precession about the total angular momentum, but the period is much too long to account for the possible precession of the jet axis discussed above.

One problem is that a three-strand braid pattern is not readily explained in terms of plasma streams from orbiting sources, unless one postulates a triple system. In addition, there is no evidence in the large-scale dynamics of NGC 4258 for a recent merger that would provide the additional black hole(s). Last, the kinematic evidence favors a substantial component of pure helical motion (§ 3.2.2), which cannot be produced in ballistic models.

4.4.2. Ejection from a Magnetized Accretion Disk

An alternative that we feel is also in conflict with certain of our data is for the helices to represent magnetized loops from a central accretion disk, which is assumed to be threaded with a poloidal magnetic field (e.g., Blandford 1990 and references therein). Instabilities resulting from rotational shear may cause magnetic flux loops to rise into the hot corona above the disk (Galeev, Rosner, & Vaiana 1979). Because the corona can generally expand as a wind, the loop is stretched outward. The magnetic field and flux-frozen gas rotate rigidly until the inertia of the gas causes the field to be bent toroidally, so dragging field lines and gas into helices. This toroidal component of the magnetic field can then collimate the outflow of the plasma. However, the observed helices cycle over of order 0.6 Myr, which exceeds any plausible dynamical time scale of the inner, magnetized portion of the accretion disk. The magnetized disk may well form part of a larger molecular torus which could extend to the hundred pc scale inferred previously for the radius of the "braiding." However, we would not expect significant magnetic loops from anchor foot points that are so far out. Moreover, a coronal wind to accelerate the loops would only be present near the base of the toroidal funnel, so it is hard to see how the braid pattern would persist to the observed scales.

4.4.3. Fluid Instabilities

Jets can be disrupted by fluid instabilities, some of which can be damped by a strong internal, axial magnetic field. Any azi-muthal field component B_φ can confine a current-carrying beam by pinching and potentially recollimating with force $\mathbf{j} \times \mathbf{B}_\varphi$. Pinch or "sausage" instabilities grow at the Alfvén speed, $v_A = B/(4\pi n)^{1/2}$ for field strength B and thermal gas density n. If we take the field strength in the bright knots to be that inferred by Hummel et al. (1989), we obtain $v_A \approx 45(B/20$ $\mu G)(1$ cm$^{-3}/n_e)^{1/2}$ km s^{-1}, which is $\leq 50(B/20$ $\mu G)$ km s^{-1} for $n \approx n_e > 0.8$ cm^{-3} (see above), so the jet outflow is almost certainly super-Alfvénic. Magnetic field topologies have been inferred from the observed polarization pattern across and along jets in powerful radio galaxies (Laing 1981) but are unconstrained in NGC 4258 because the jet strands are unresolved in existing polarization maps. Van der Kruit et al. (1972) note that the total synchrotron luminosity of NGC 4258 is not abnormally high for a galaxy of its Hubble type, suggesting that the magnetic field in the galaxy is not unusually large (see also Hummel et al. 1989). A relatively small compression of a preexisting magnetic field in the disk can account for the synchrotron emission of the jet. The internal field of a low-power radio source like NGC 4258 is thus, arguably, of secondary importance to the hydrodynamics. Nevertheless, the magnetic pressure of $\approx 3 \times 10^{-11}$ ergs cm^{-3} may be comparable to the gas pressure of $\approx 3 \times 10^{-11}(n_e/10$ cm$^{-3})(T/20,000$ K). In what follows we shall therefore ignore disruptions associated with a strong internal magnetic field, such as the pinch and "firehose" instabilities. A high-resolution radio map would allow the magnetic field strength and topology on the scale of the width of the braids to be mapped directly.

In the linear stability analysis of weakly magnetized beams, the only perturbations capable of spatially displacing the strand centers in the observed manner are the $n = \pm 1$ "kink" or "helical" modes (Birkinshaw 1991), which are favored at higher internal Mach numbers. The amplitude of these motions in the SE jet complex may be larger than can be handled by the linear theory (which is restricted to motions that generate pressure variations $\partial P/P \ll 1$). However, it is generally assumed that the theory can identify which modes survive to grow into the observed, nonlinear regime. Analysis shows that a single mode grows fastest and dominates the instabilities. Practitioners of instability analysis seem to agree that large-amplitude oscillations require an external driving mechanism, such as precession or orbital evolution, to amplify a single mode.

Birkinshaw (1984, 1991) has calculated the growth rate of Kelvin-Helmholtz instabilities for nonmagnetized beams and has discussed their relevance to wiggling jets in radio sources. We suspect that such instabilities play a significant role in the structure of the jets of NGC 4258. However, we have not applied the linear theory to these jets because of Birkinshaw's pessimistic assessment of the reliability of the linear analysis, based on the ambiguities of its previous application to systems with much more complete radio data than currently exist for NGC 4258. He convincingly demonstrates that the results are critically sensitive to poorly constrained parameters of the jet flow, in particular to the structure of the shear layer between jet and ambient ISM, which the current theoretical formulation drastically simplifies as a "vortex sheet" (see § 6.5 in Birkinshaw 1991 for details).

The overall width of the SE jet in NGC 4258 is ≈ 400 pc (e.g., Fig. 11a), which is larger than the typical z-thickness of the gas disk in a spiral galaxy. Because the jet is close to the disk plane, it must be subject to a strong z gradient of ram pressure from the normally rotating interstellar gas. It is intriguing that the

inferred azimuthal velocity is comparable to or larger than the disk rotation velocity (cf. Fig. 14a). Such differential ram pressure would presumably tend to disrupt the jet and, in common with other instabilities, does not readily account for the apparently well-defined wavelength of the braiding (Fig. 15). Nevertheless, it may be that some of the helical structure results from a periodic entrainment of material as the jet traverses denser regions of the interstellar gas disk (§ 4.5).

Further quantification of the jet/ISM interaction and isolation of possible hydrodynamic and MHD instabilities will require accurate thermal pressures to complement our kinematic and flux maps, more sensitive density constraints, and explicit simulation of the bar shocks in the disk. Polarization data at high radio frequencies, with resolution <1″, will establish directly the magnetic field structure and the degree of mixing between thermal and relativistic particles. It will be of great interest to combine these data with our kinematic constraints on the three dimensional structure of the jets to interpret the projected distributions of radio polarization, spectral index, and synchrotron intensity in terms of plausible magnetic field topologies (Laing 1981).

4.5. Entrainment

The SE helices have only $\approx 10^6\ M_\odot$ (1 cm$^{-3}/n_e$) of ionized gas (§ 2.1) distributed along a 10 kpc arc length (after allowing for braiding), to yield an average linear mass density of 100 $M_\odot$, so only $\approx 0.1\ M_\odot$ yr^{-1} must be entrained and ionized along the entire jet. For the NNW jet, MRNL use the results of simulations by De Young (1986) to show that entrainment of the ambient ISM (with an average density of 1 cm^{-3}) is energetically plausible. Given that our derived ionized masses are $\approx 1/15$ of the values used by MRNL for similar densities, and that VA found no H I enhancements along the anomalous arms, disk entrainment indeed seems plausible. We are less sanguine about using these calculations to estimate actual entrainment rates. More recent slab simulations (Christiansen & Schiano 1992) indicate that entrainment rates between two media with a large density contrast have been overestimated in computations because of limited grid resolution. The strong mismatch in sound speeds prevents the two media from mixing. In contrast, the change in jet momentum at a jet/cloud deflection is transported through the cloud as a supersonic shock, and PLRMN argue persuasively that this has occurred N of the nucleus. If the flow on the NNW side is loaded by molecular gas, Kelvin-Helmholtz instabilities grow faster,

entraining more material. The radio emission would then increase on this side, as is observed (van der Kruit et al. 1972).

5. SUMMARY

Our observations of NGC 4258 have clarified several dynamical issues. We have attempted to quantify elliptical streaming in the barred disk. We stress that this procedure will only have a dynamical basis once the surface photometry has been combined with our kinematics to produce a self-consistent mass model. Nonetheless, it is already clear that the *mean* velocities of ionized gas associated with the jets deviate by at most 60 km s^{-1} along the line of sight, which may be compared to the ≈ 25 km s^{-1} radial motions that result from the bar-forced streaming. We have kinematically isolated the jet flow NNW of the nucleus, and confirmed a vigorous interaction between this jet and molecular gas in the inner 0.6 kpc radius of the galaxy. The active flow to the NNW is actually displaced 5″ from where others have located it and is not enhanced in Hα relative to its surroundings during its passage through the dense gas disk.

The braided jet SE of the nucleus is the most spectacular aspect of the outflow. We infer the existence of three tightly wrapped strands, which "open out" close to the turnover point of the disk rotation curve. This jet is a resolved source of X-ray emission, with thermal bremsstrahlung the likely mechanism. The helical, braided structure is seen in *both* images and velocity maps, providing evidence for motion *along* the strands, and suggesting that the braid pattern is driven by fluid instabilities. The nature of the braiding is unclear, but the pattern may be related to fluid instabilities in the jet–ISM boundary layer. Shear may be important in amplifying the ambient magnetic field and in exciting unstable Kelvin-Helmholtz modes that may produce the helices. Motion along a strong helical magnetic field seems less likely, but high-resolution, radio observations are needed to map the field's direction and magnitude, on the scale of the braids, to explore the possible role of magnetic flux tubes.

REFERENCES

Begelman, M. C., Blandford, R. D., & Rees, M. J. 1980, Nature, 287, 307
Birkinshaw, M. 1984, MNRAS, 208, 887
———. 1991, in Beams and Jets in Astrophysics, ed. P. A. Hughes (New York: Cambridge Univ. Press), § 6.5
Bland, J., & Tully, R. B. 1989, AJ, 98, 723
Bland-Hawthorn, J., Wilson, A. S., & Tully, R. B. 1991, ApJ, 371, L19
Blandford, R. D. 1990, in Active Galactic Nuclei, ed. T. J.-L. Courvoisier & M. Mayor (New York: Reidel), § 4.2
Cecil, G. 1991, PASP, 103, 894
Cecil, G., Bland, J., & Tully, R. B. 1990, ApJ, 355, 70
Christiansen, W., & Schiano, A. V. R. 1992, in preparation
Claussen, M. J., Heiligman, G. M., & Lo, K. Y. 1984, Nature, 310, 298
Dettmar, R. J., & Koribalski, B. 1990, A&A, 240, L15
De Young, D. S. 1986, ApJ, 307, 62
Fabbiano, G., Kim, D.-W., & Trinchieri, G. 1992, ApJS, in press
Filippenko, A. V., & Sargent, W. L. W. 1985, ApJS, 57, 503
Ford, H. C., et al. 1986, ApJ, 311, L7
Galeev, A. A., Rosner, R., & Vaiana, G. S. 1979, ApJ, 229, 318
Hummel, E., Krause, M., & Lesch, H. 1989, A&A, 211, 266
Icke, V. 1991, in Beams and Jets in Astrophysics, ed. P. A. Hughes (New York: Cambridge Univ. Press), § 5.3
Laing, R. A. 1981, ApJ, 248, 87
Martin, P., Roy, J-R., Noreau, L., & Lo, K. Y. 1989, ApJ, 345, 707 (MRNL)

Osterbrock, D. E. 1989, Astrophysics of Gaseous Nebulae and Active Galactic Nuclei (Mill Valley, CA: Univ. Science Books)
Plante, R., Lo, K. Y., Roy, J.-R., Martin, P., & Noreau, L. 1991, ApJ, 381, 110 (PLRMN)
Press, W. H., & Teukolsky, S. A. 1990, Comput. Phys., 4, 699
Roberts, M. S., Huntley, J. M., and van Albada, G. D. 1979, ApJ, 233, 67
Rubin, V. C., & Graham, J. A. 1990, ApJ, 362, L5
Rybicki, G. B., & Lightman, A. P. 1979, Radiative Processes in Astrophysics (New York: Wiley), § 5.2
Stauffer, J. R. 1982, ApJ, 262, 166
Staveley-Smith, L., et al. 1990, ApJ, 364, 23
Teuben, P. J., & Sanders, R. H. 1985, MNRAS, 212, 257
Tully, R. B. 1988, Nearby Galaxies Catalog (New York: Cambridge Univ. Press)
van Albada, G. D. 1978, Ph.D. thesis, Univ. of Leiden
———. 1980, A&A, 90, 123 (VA)
van Albada, G. D., & van der Hulst, J. M. 1982, A&A, 115, 263
van der Kruit, P. C. 1974, ApJ, 192, 1
van der Kruit, P. C., & Allen, R. J. 1978, ARA&A, 16, 103
van der Kruit, P. C., Oort, J. H., & Mathewson, D. S. 1972, A&A, 21, 169
Wilson, A. S., & Heckman, T. M. 1985, in Astrophysics of Active Galaxies and Quasi-Stellar Objects, ed. J. S. Miller (Mill Valley, CA: Univ. Science Books), 39